日本磁気学会
ISSN 2432-0250
Journal of the Magnetics Society of Japan
Electronic Journal URL: https://www.jstage.jst.go.jp/browse/msjmag

Vol.45 No.3 2021

Journal

JOURNAL OF THE MAGNETICS SOCIETY OF JAPAN

Vol.45 No.3 2021

日本磁気学会

ISSN 2432-0250

HP: http://www.magnetics.jp/ e-mail: msj@bj.wakwak.com

Electronic Journal: http://www.jstage.jst.go.jp/browse/msjmag

Journal of the Magnetics Society of Japan
Vol. 45, No. 3

Electronic Journal URL: https://www.jstage.jst.go.jp/browse/msjmag

CONTENTS

J. Magn. Soc. Jpn., **45**, 50-55 (2021)

<Paper>

Performance Improvement of Spoke-shaped Interior Permanent Magnet Magnetic Gear

Y. Mizuana, K. Nakamura, Y. Suzuki*, Y. Oishi*, Y. Tachiya*, and K. Kuritani*

Graduate School of Engineering, Tohoku University, *6-6-11 Aoba Aramaki Aoba-ku, Sendai, Miyagi 980-8579, Japan*

*Prospine Co., Ltd., *117 Shinsengarida, Matsuyamatsugihashi, Osaki, Miyagi 987-1305, Japan*

Magnetic gears have several advantages such as having low acoustic noise and being maintenance-free because there is no mechanical contact. Among these gears, the flux-modulated type has a higher torque density and efficiency than the other types. Therefore, it is expected to be put into practical use. In previous papers, a spoke-shaped interior permanent magnet (IPM) rotor structure was proposed in order to reduce the eddy current loss in magnets. This paper presents three methods for improving the performance of the spoke-shaped IPM magnetic gear. First, the position of the magnetic bridges is changed from the air gap side to the back yoke side to increase the effective magnetic flux. Second, amorphous alloy is used for the rotor core and pole pieces in order to reduce iron loss. Third, bonded Nd-Fe-B magnets for canceling the leakage flux are arranged to sandwich the inner rotor from both sides. As a result of prototype tests, the measured maximum torque of the proposed spoke-shaped IPM magnetic gear was 44% higher than that of the conventional one. In addition, the measured maximum efficiency reached 99.85% at 100 rpm.

Key words: magnetic gear, interior permanent magnet (IPM), cancel magnet, amorphous alloy, magnetic bridge

1. Introduction

Mechanical gears are one of the most important mechanical elements. Thus, they are widely used in various fields such as industry, transportation, and power generation. However, the mechanical gears have several problems including acoustic noise and vibration due to mechanical contact. Furthermore, they require lubricant for cooling and wear reduction, and periodic maintenance.

On the other hand, magnetic gears change speed and transmit torque without any mechanical contacts. Therefore, they have several advantages of low acoustic noise, low vibration, and maintenance-free compared to mechanical gears. In previous researches [1)-3)], various types of magnetic gears have been introduced. Among them, a flux-modulated type magnetic gear [4)-5)] has attracted attention recently.

Fig. 1 shows a basic structure of flux-modulated type magnetic gear. It consists of the inner and outer rotors and pole pieces placed between the both rotors. This magnetic gear works as a gear when the magnet flux is modulated by pole pieces. Since all the magnets of the inner and outer rotors contribute to torque transmission, a flux-modulated type magnetic gear has higher torque density and efficiency than the other types [6)-7)].

For the practical use of a flux-modulated type magnetic gear, further torque improvement and loss reduction are necessary. In previous papers [8)-9)], a spoke-shaped interior permanent magnet (IPM) magnetic gear was proposed for the reduction of eddy current loss in magnets caused by asynchronous harmonic fluxes.

This paper presents three ideas to improve the performance of the spoke-shaped IPM magnetic gear. First, some problems with conventional spoke-shaped IPM magnetic gear are pointed out. Next, solutions to the above problems are proposed and evaluated by using JMAG-Designer ver. 19.1, which is general-purpose finite element method (FEM) software. Finally, in order to prove the validity, prototype tests are demonstrated.

2. Performance improvement of the spoke-shaped IPM magnetic gear

2.1 Problems of conventional spoke-shaped IPM magnetic gear

Fig. 2 shows specifications of conventional spoke-shaped IPM magnetic gear. The diameter and axial length are 150 mm and 25 mm, respectively. The numbers of pole-pairs of the inner and outer rotor are 3 and 31, respectively. Hence, the gear ratio is 10.33, which is given by the ratio of the inner and outer pole-pairs [4)]. The number of pole pieces is 34 given by the sum of the numbers of the inner and outer pole-pairs [4)]. The inner and outer magnets are embedded in the inner and outer rotor core as a spoke shape. Both rotors have 1 mm-wide magnetic bridges on the air gap side. Non-magnetic stainless steel is used

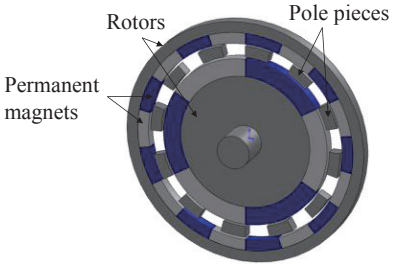

Fig. 1 Basic structure of flux-modulated type magnetic gear.

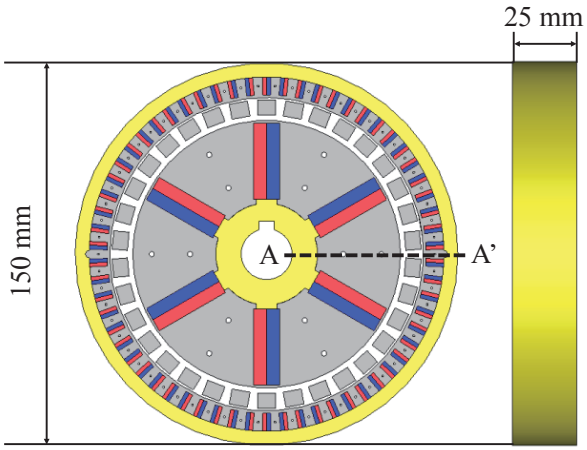

Bridge position	Air gap side
Bridge width	1 mm
Cancel magnets	Not included
Air gap	2 mm (inner) 1 mm (outer)
Inner pole-pairs	3
Outer pole-pairs	31
Number of pole pieces	34
Gear ratio	10.33
Core material	35A250
Pole-piece material	SMC
Magnet material	Sintered Nd-Fe-B

Fig. 2 Specifications of conventional spoke-shaped IPM magnetic gear.

for the rotor back yoke to prevent a short circuit of the PM flux. Core material of the both rotors is non-oriented silicon steel with a thickness of 0.35 mm (35A250), while that of pole-pieces is soft magnetic composite (SMC).

Fig. 3 (a) illustrates a vector diagram of magnetic flux density of conventional spoke-shaped IPM magnetic gear. From the figure, it is understood that a part of the PM flux flows through the magnetic bridges, which leads to reduction of effective PM flux.

Fig. 3 (b) indicates losses of conventional spoke-shaped IPM magnetic gear calculated by 3D-FEM. As shown in the figure, the eddy current loss in the magnets is very small due to the spoke-shaped IPM rotor structure, while the iron loss is large. For improvement of efficiency, the reduction of iron loss is critical.

Fig. 3 (c) shows leakage flux of conventional spoke-shaped IPM magnetic gear (A-A' cross section in Fig. 2). From the figure, it is clear that the axial leakage flux is more severe in the inner rotor than the outer rotor because the larger size magnets are arranged facing each other. It is concerned that the axial leakage flux induces eddy current in the gear housing and decreases the efficiency.

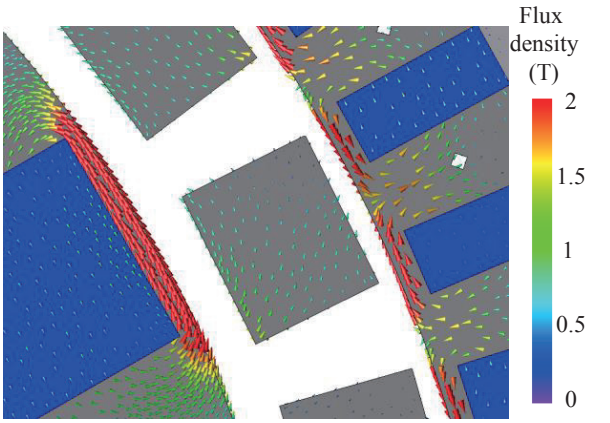

(a) Vector diagram of magnetic flux density of conventional spoke-shaped IPM magnetic gear.

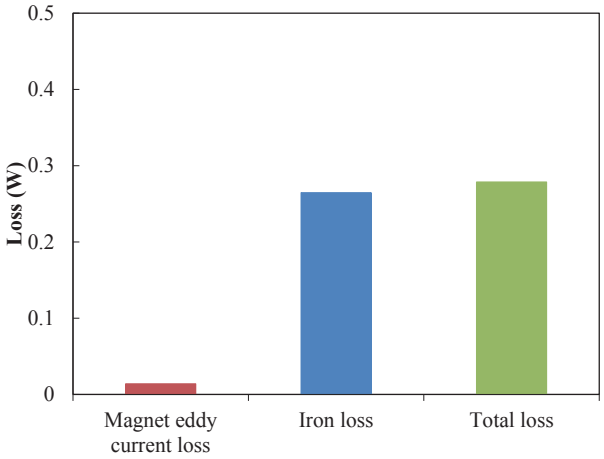

(b) Losses of conventional spoke-shaped IPM magnetic gear calculated by 3D-FEM.

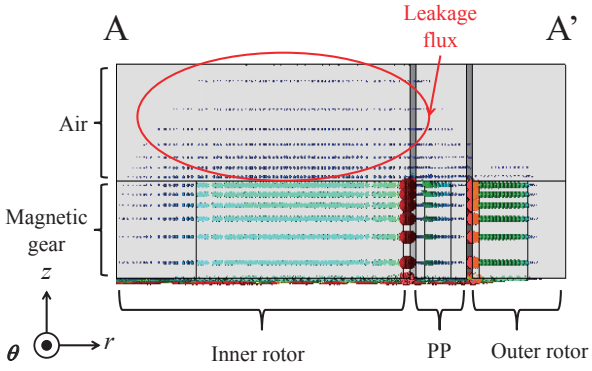

(c) Leakage flux distribution of conventional spoke-shaped IPM magnetic gear (A-A' cross section in Fig. 2).

Fig. 3 Problems with conventional spoke-shaped IPM magnetic gear.

2.2 Methods for performance improvement

Fig. 4 shows specifications of proposed spoke-shaped IPM magnetic gear. For the performance improvement, three ideas are employed for the proposed magnetic gear.

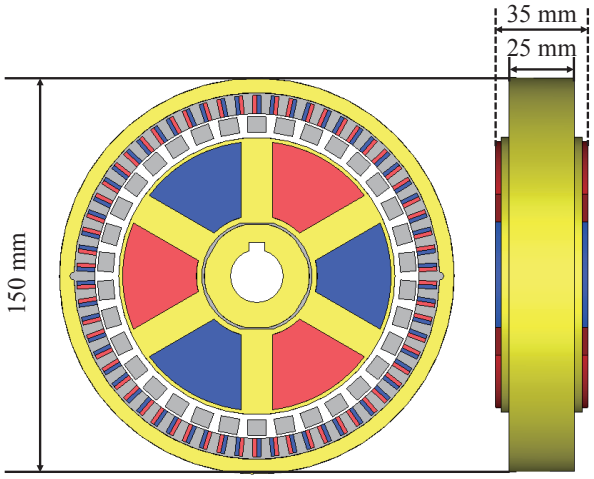

Bridge position	Back yoke side
Bridge widths	2 mm (inner) 1 mm (outer)
Cancel magnets	Included (5mm)
Air gap	2 mm (inner) 1 mm (outer)
Inner pole-pairs	3
Outer pole-pairs	31
Number of pole pieces	34
Gear ratio	10.33
Core material	Amorphous alloy
Pole-piece material	Amorphous alloy
Magnet material	Sintered Nd-Fe-B

Fig. 4 Specifications of proposed spoke-shaped IPM magnetic gear.

First, for increasing the effective PM flux, the position of the magnetic bridges is changed from the air gap side to the back yoke side as shown in Fig. 5. Fig. 6 indicates magnetic flux density waveforms in outer air gap. From the figure, it is understood that the magnetic flux in outer air gap is increased by arranging the magnetic bridges on the back yoke side.

Second, in order to reduce iron loss, amorphous alloy is used for the inner and outer rotor core, and pole pieces. Fig. 7 shows comparison of total loss when the inner rotor rotates at 300 rpm. As shown in the figure, it is revealed that the total loss of the proposed magnetic gear can be significantly reduced by employing amorphous alloy for pole pieces.

Third, bonded Nd-Fe-B magnets for canceling the axial leakage flux are arranged to sandwich the inner rotor from both sides as shown in Fig. 8. These cancel magnets are magnetized in the opposite direction to the axial leakage flux and fixed by the stainless steel frame. The thickness of the cancel magnets was optimized to 5 mm so that the average axial leakage flux on surface of cancel magnets is zero as shown in Fig. 9.

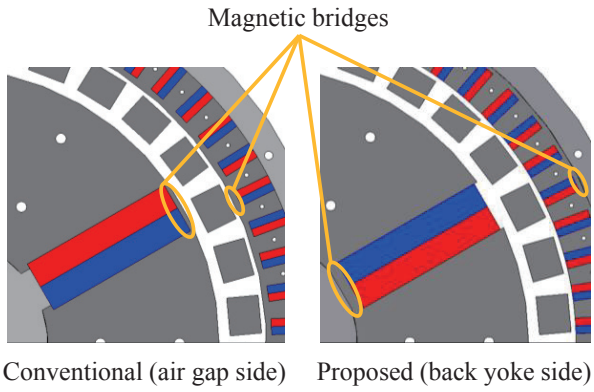

Fig. 5 Position of magnetic bridges of conventional and proposed spoke-shaped IPM magnetic gears.

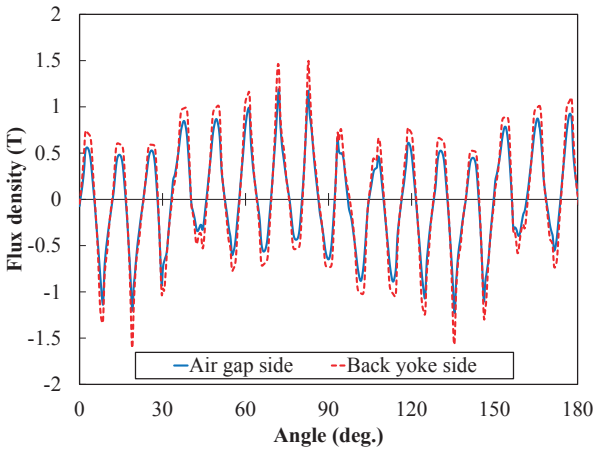

Fig. 6 Magnetic flux density waveforms in outer air gap.

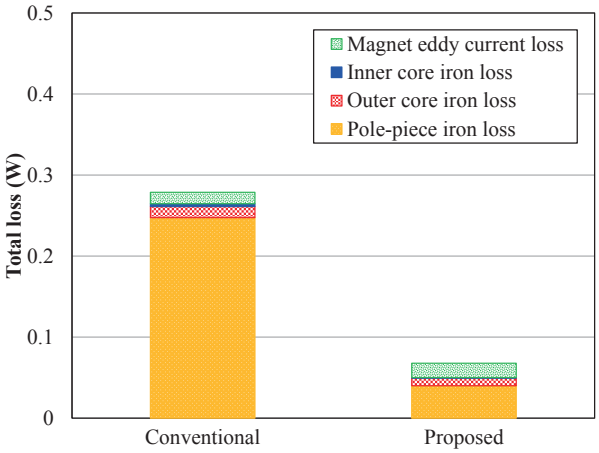

Fig. 7 Comparison of calculated total loss when inner rotational speed was 300 rpm.

Fig. 10 indicates the radial magnetic flux density waveforms in inner air gap with and without cancel magnets. From, the figure, it is understood that the magnetic flux in inner air gap is enhanced by the cancel magnets. Therefore, the cancel magnets are expected to contribute to the torque improvement in addition to canceling the axial leakage flux.

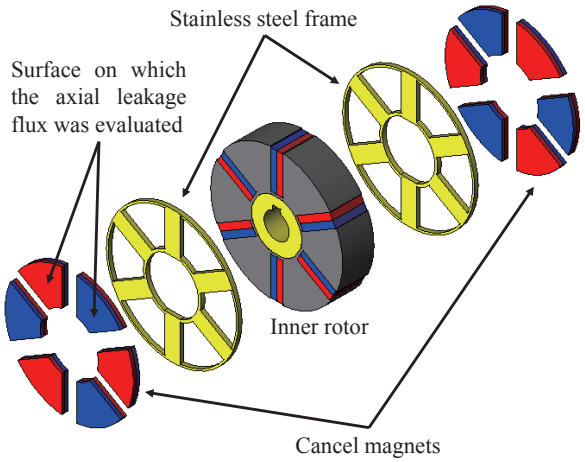

Fig. 8 Exploded view of inner rotor with cancel magnets.

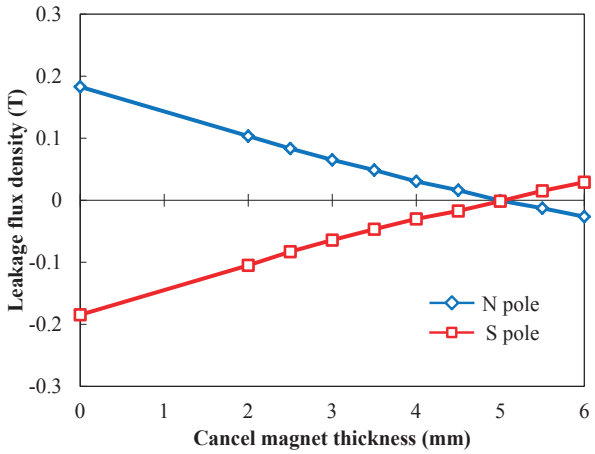

Fig. 9 Calculated average axial leakage flux density on surface of cancel magnets.

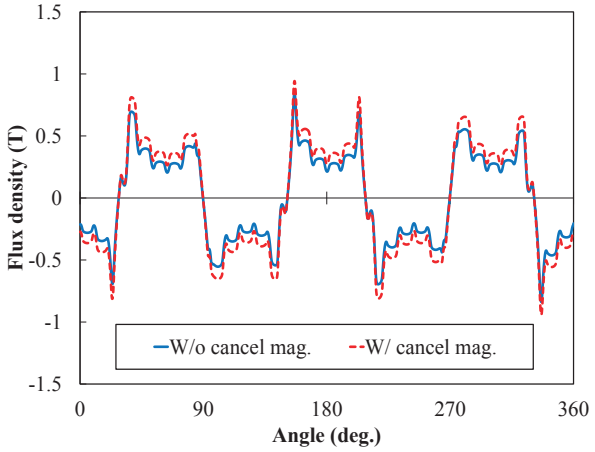

Fig. 10 Calculated radial magnetic flux density waveforms in inner air gap with and without cancel magnets.

Fig. 11 shows comparison of the maximum torque when a rotational speed of the inner rotor is 300 rpm. The figure reveals that the maximum torque of the proposed magnetic gear is larger than that of the conventional one, and that amorphous alloy also contributes to the torque improvement despite low saturation magnetic flux density.

To clarify the above reason, Fig. 12 (a) and Fig. 12 (b) indicate contour diagrams of magnetic flux density when the rotor core materials are 35A250 and amorphous alloy, respectively. Pole piece material is SMC in both cases. As shown in the figure, it is clear that the magnetic bridges are magnetically saturated at lower magnetic flux density when amorphous alloy is used for the rotor core, which increases the effective PM flux, and results in the improvement of torque.

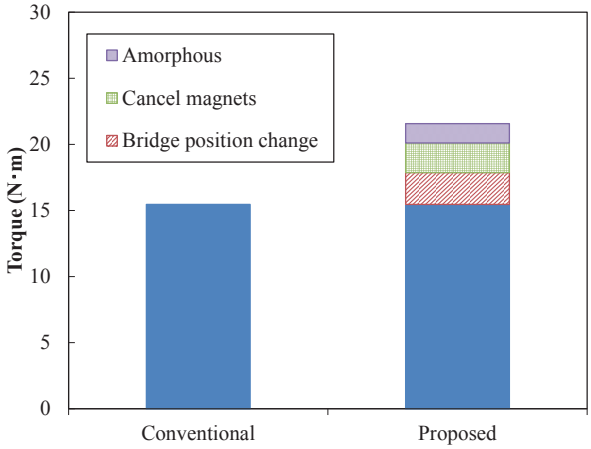

Fig. 11 Comparison of calculated maximum torque.

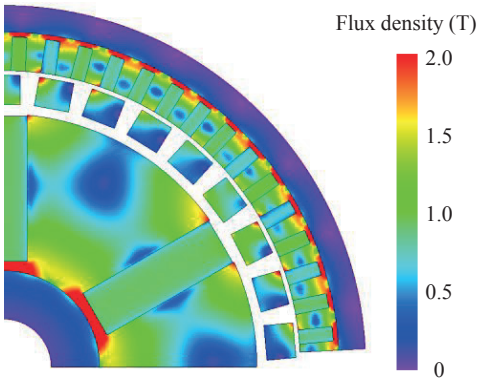

(a) Non-oriented silicon steel (35A250)

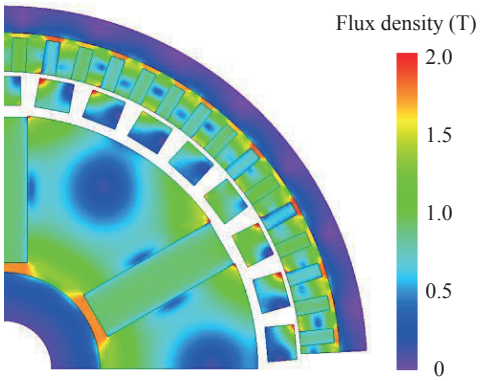

(b) Amorphous alloy

Fig. 12 Contour diagrams of magnetic flux density.

3. Prototype tests of spoke-shaped IPM magnetic gear

Based on the simulation results of the previous chapter, the proposed spoke-shaped IPM magnetic gear was prototyped and its performance was compared with that of the conventional one.

First, the effect of the cancel magnets is verified. Fig. 13 shows the experimental setup for measuring leakage flux. The axial leakage flux is measured with a Gauss meter at the five points shown in Fig. 14.

Table 1 indicates the measured axial leakage flux with and without the cancel magnets. From the table, it is proved that the axial leakage flux can be remarkably reduced by the cancel magnets.

Fig. 15 shows appearance of prototyped spoke-shaped IPM magnetic gear. As shown in the figure, it has an observation hole for measuring the leakage flux and the temperature inside the prototype gear. The gear housing is made of fiber reinforced plastic (FRP) in order to prevent generation of losses caused by stray electromagnetic field.

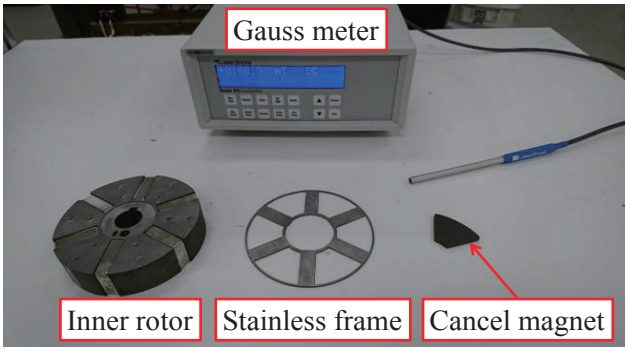

Fig. 13 Experimental setup for measuring leakage flux.

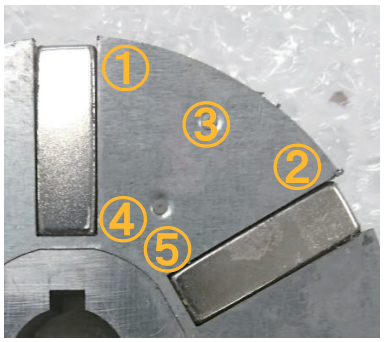

Fig. 14 Measured points.

Table 1 Measured leakage flux density.

Measured point	W/o cancel magnets	W/ cancel magnets
1	0.229 T	0.005 T
2	0.262 T	0.001 T
3	0.144 T	0.006 T
4	0.243 T	0.012 T
5	0.258 T	0.012 T

Fig. 16 indicates the experimental system for prototyped magnetic gear. In this system, the prototype magnetic gear operates as a step-up gear. The rotational speed of the outer rotor is regulated at an arbitrary speed by the servomotor. The load torque is controlled by the hysteresis brake.

Fig. 17 shows comparison of the torque behavior at a constant speed of the inner rotor of 300 rpm. As shown in the figure, the load torque is increased stepwise until the magnetic gear is stepped out. The figure reveals that the measured maximum torque of the proposed spoke-shaped IPM magnetic gear is 44% higher than that of the conventional one. On the other hand, the measured torque is about 10% lower than the calculated one. This is because magnetic flux leaks more than expected by FEM. In IPM magnetic gear, the same poles of the inner and outer magnets face each other so that magnetic flux flows toward the pole pieces. However, not all of the magnetic flux flows toward the pole piece, and some flux leaks in various directions. In addition, flat structure shown in Fig. 2 contributes to increasing the leakage flux. For these reasons, effective magnetic flux decreases, and the measured torque is smaller.

Fig. 18 shows comparison of the measured efficiency at a constant speed of the inner rotor of 300 and 100 rpm, respectively. The figure demonstrates that the efficiency of the proposed spoke-shaped IPM magnetic gear is remarkably improved, and the measured maximum efficiency of the proposed spoke-shaped IPM magnetic gear reaches 99.85% at an inner rotor speed of 100 rpm.

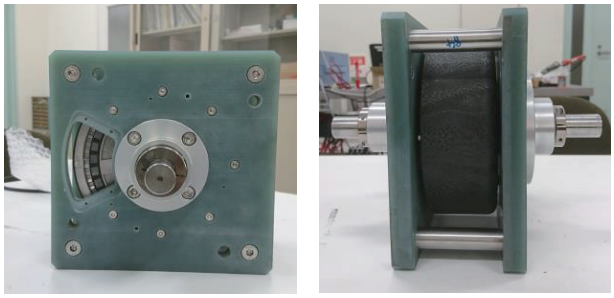

Fig. 15 Appearance of prototyped spoke-shaped IPM magnetic gear.

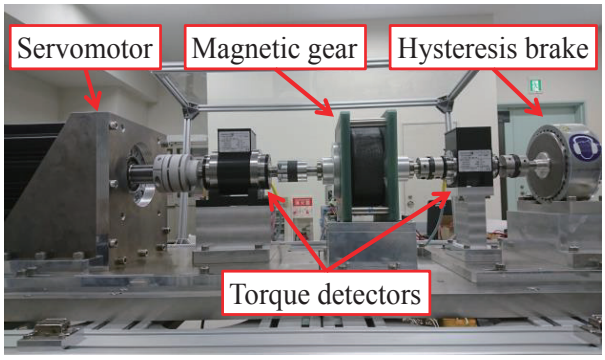

Fig. 16 Experimental system for prototyped magnetic gear.

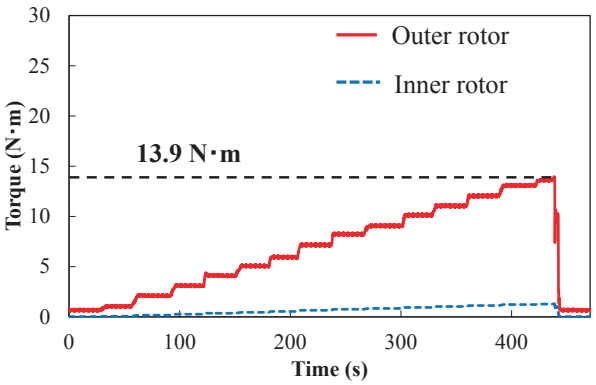

(a) Conventional spoke-shaped IPM magnetic gear.

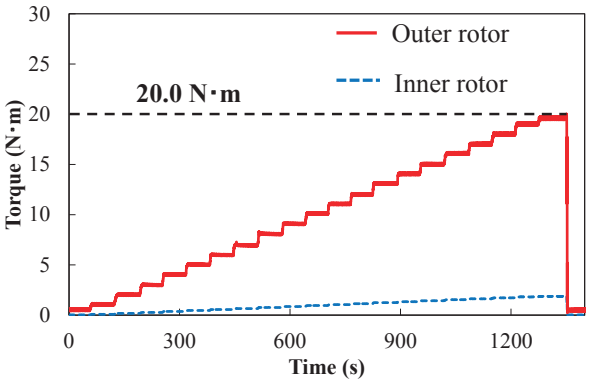

(b) Proposed spoke-shaped IPM magnetic gear.

Fig. 17 Measured torque behavior of conventional and proposed spoke-shaped IPM magnetic gears.

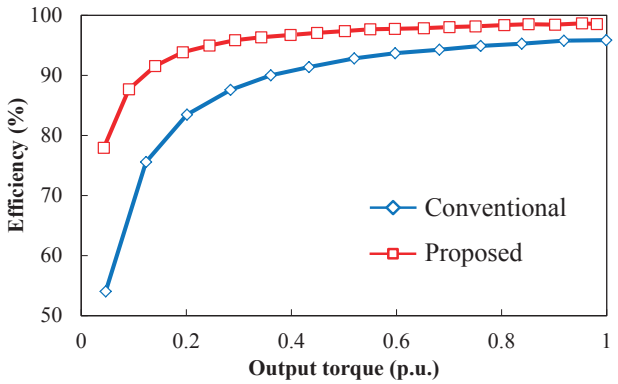

(a) Inner rotational speed : 300 rpm

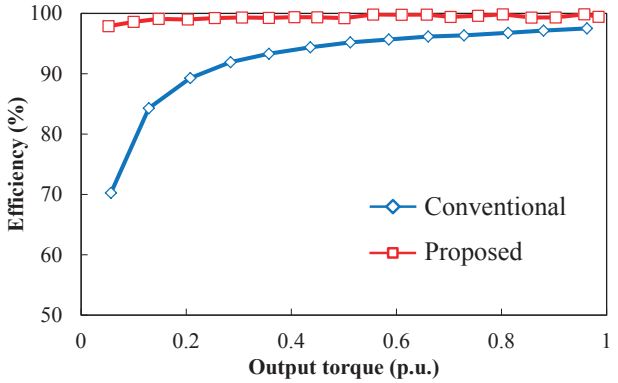

(b) Inner rotational speed : 100 rpm

Fig. 18 Measured efficiency of conventional and proposed spoke-shaped IPM magnetic gears.

4. Conclusion

This paper presented three methods for improving the performance of the spoke-shaped IPM magnetic gear. First, a position of magnetic bridges is changed from the air gap side to the back yoke side. Second, amorphous alloy is employed for rotor cores and pole pieces. Third, bonded Nd-Fe-B magnets are arranged to sandwich the inner rotor from both sides in order to cancel the axial leakage flux.

From the simulation results, it was revealed that all three methods are effective in the performance improvement of the spoke-shaped IPM magnetic gear.

In the prototype tests, the axial leakage flux was reduced by more than 95% by using the cancel magnets. Furthermore, it was demonstrated that the proposed spoke-shaped IPM magnetic gear has 44% larger torque than the conventional one, and the measured maximum efficiency reaches 99.85% at an inner rotational speed of 100 rpm.

Acknowledgements This work was supported in part by the WISE Program for AI Electronics, Tohoku University.

References

1) T. B. Martin, Jr.: U.S. Patent, 3, 378, 710 (1968).
2) D. E. Hesmondhalgh and D. Tipping: *IEE Proc. B, Elect. Power Appl.*, **127**, 129 (1980).
3) K. Tsurumoto and S. Kikushi: *IEEE Trans. Magn.*, **23**, 3622 (1987).
4) K. Atallah and D. Howe: *IEEE Trans. Magn.*, **37**, 2844 (2001).
5) F. T. Jørgensen, P. O. Rasmussen, and T. O. Andersen: *Summer Seminar on Nordic Network for Multi Disciplinary Optimized Electric Drives* (2003)
6) T. Ikeda, K. Nakamura, and O. Ichinokura: *J. Magn. Soc. Jpn.*, **33**, 130 (2009) (in Japanese).
7) M. Fukuoka, K. Nakamura, and O. Ichinokura: *IEEJ Trans. A*, **134**, 416 (2014) (in Japanese).
8) T. Ikeda, K. Nakamura, and O. Ichinokura: *J. Magn. Soc. Jpn.*, **34**, 380 (2010) (in Japanese).
9) Y. Mizuana, K. Nakamura, Y. Suzuki, Y. Oishi, Y. Tachiya, and K. Kuritani: *International Journal of Applied Electromagnetics and Mechanics* (2020).

Received Dec. 07, 2020; Accepted Jan. 26, 2021

J. Magn. Soc. Jpn., **45**, 56-60 (2021)

<Paper>

A Consideration of Magnetostriction Force Calculation for Transformer Core by Using Reluctance Network Analysis

Y. Hane, K. Nakamura, and N. Kurita*

Graduate School of Engineering, Tohoku Univ., *6-6-11 Aoba Aramaki, Aoba-ku, Sendai 980-8579, Japan*

*Hitachi, Ltd., *7-1-1 Omikacho, Hitachi 319-1292, Japan*

In recent years, it has been strongly required to reduce radiated noises from transformer cores used in electric power systems. The noises from transformer cores seem to be mainly caused by magnetostriction. Thus, it is necessary to establish a method for quantitatively calculating the force generated from the magnetostriction (magnetostriction force) with not only high-accuracy but also high-speed. This paper presents that the magnetostriction force is calculated based on a reluctance network analysis (RNA) by using a simple-shape wound core as an object of discussion. The validity of the proposed method is indicated by comparing with calculation results obtained from a finite element method (FEM).

Key words: finite element method (FEM), magnetostriction force, reluctance network analysis (RNA)

1. Introduction

In recent years, it is strongly required to reduce noises radiated from transformers used in electric power systems. The causes of a noise of electric machines are mainly divided into the electromagnetic force and the magnetostriction generated in an iron core. Among them, the magnetostriction is considered to be the major cause of the noise for transformers[1]. Therefore, in order to reduce the acoustic noise due to the magnetostriction for transformers, it is necessary to establish a method for calculating the force generated from the magnetostriction (magnetostriction force). However, it is difficult to theoretically analyze the magnetostriction such as based on micromagnetics. To overcome this problem, Kitagawa *et al.* [2] presented the method which calculates the magnetostriction force by using the magnetic flux density distribution obtained from a finite element method (FEM), and the magnetic flux density versus magnetostriction characteristics of the core material obtained from the measurement.

However, in order to design and analyze transformers for the purpose of acoustic noise reduction, it is essential to calculate displacement of a shape of an iron core by structural analysis, and the radiated sound by acoustic analysis, based on the magnetostriction force obtained from electromagnetic field analysis. It leads the analytical model to be very large, which requires a long calculation time and a huge computer capacity. Therefore, in order to realize electromagnetic-structural-acoustic coupled analysis, the analytical model should be simple as well as with high calculation accuracy.

To solve the above problem, this paper presents that the calculation method of the magnetostriction force proposed in the reference 2) is applied to a reluctance network analysis (RNA). The RNA expresses an analytical object by one reluctance network. All the reluctances can be determined by *B-H* curve of the material and dimensions [3]. The RNA has some advantages such as a simple model, fast calculation, and easy coupling with external electric circuits and motion equation. The RNA has been applied to the calculation of characteristics of various electric machines including transformers and motors [4)-6)]. In this paper, the validity of the proposed method is proved by comparing with the calculation results obtained from a two-dimensional (2-D) FEM.

Corresponding author: Y. Hane (e-mail: yoshiki.hane@ecei.tohoku.ac.jp).

2. Reluctance Network Analysis

In this chapter, a method for deriving a 2-D RNA model of a wound core made of an amorphous alloy, which is generally used for transformers, is explained.

First, the analytical object is divided into multiple elements as shown in Fig. 1(a). Here, the core is divided into 3 in the thickness direction and 16 in the rolling direction, respectively. Each divided element can be expressed in a 2-D unit magnetic circuit as shown in Fig. 1(b). Each reluctance can be determined in consideration of the nonlinear magnetic characteristics. Here, the magnetic nonlinearity is given by

$$H = \alpha_1 B + \alpha_m B^m \tag{1}$$

where the coefficients are α_1 = 2.21 and $\alpha_m = 4.88 \times 10^{-4}$, respectively. The order m = 15 is determined by the strength of the nonlinearity of the *B-H* curve. Fig. 2 shows the measured *B-H* curve of the core material and its approximated curve.

From the equation (1), the relationship between the magnetomotive force (MMF) f_m and the magnetic flux ϕ in each reluctance can be expressed by the following equation:

$$f_m = \left(\frac{\alpha_1 l}{S} + \frac{\alpha_m l}{S^m} \phi^{m-1} \right) \phi \tag{2}$$

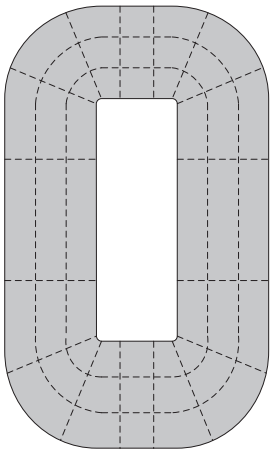

(a) Division of a wound core.

(b) Unit magnetic circuit.

Fig. 1 Division of a wound core based on RNA.

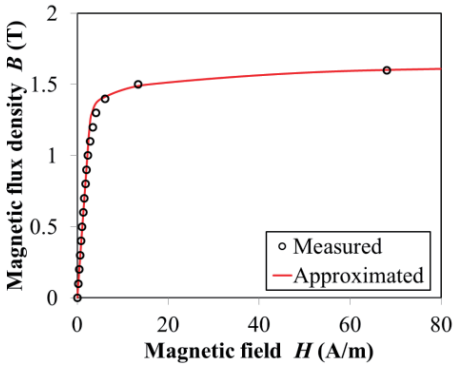

Fig. 2 *B-H* curve of core material and its approximated curve.

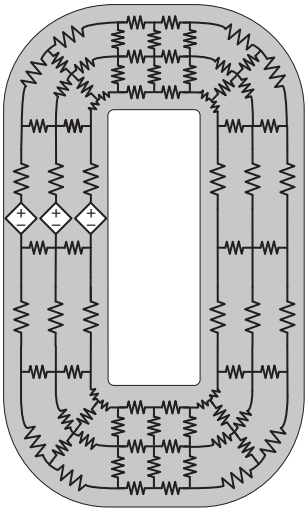

Fig. 3 Schematic diagram of a 2-D RNA model of a wound core.

where the average cross-sectional area and magnetic path length of each element are S and l, respectively. Therefore, the nonlinear reluctance R_m is given by the following equation:

$$R_m = \frac{\alpha_1 l}{S} + \frac{\alpha_m l}{S^m}\phi^{m-1} \tag{3}$$

Here, it is assumed that the magnetic properties of the core are isotropic for simplicity.

Fig. 3 shows a schematic diagram of the derived 2-D RNA model of the wound core. The MMFs are generated from the winding current.

3. Calculation Method for Magnetostriction Force

As mentioned above, it is difficult to theoretically calculate the magnetostriction force. Therefore, in this paper, the magnetostriction force is calculated by using the measured values of the magnetic flux density versus magnetostriction characteristics of the core material, based on the method proposed in the reference 2). The magnetic flux distribution of the core can be obtained from the RNA. In this chapter, first, the magnetic flux density versus magnetostriction characteristics used for the analysis are shown. Next, the calculation method of the magnetostriction force for the RNA is described.

3.1 Magnetic flux density versus magnetostriction characteristics

In general, it is difficult to measure the magnetostriction from the amorphous alloy because its thickness is very thin. Thus, in this paper, the alternative data is created by correcting the peak-to-peak value of the magnetostriction curve of the grain-oriented silicon steel [7] to 27 ppm which is nominal value of the magnetostriction of the amorphous alloy. Fig. 4 shows the corrected magnetic flux density versus magnetostriction characteristics used as a look-up table in the analysis.

3.2 Calculation method for magnetostriction force

The magnetostriction force applied to the edges of each element is expressed by the following equation, based on the Hooke's law.

$$\boldsymbol{p} = \int_S \boldsymbol{D}\boldsymbol{\varepsilon} dS \tag{4}$$

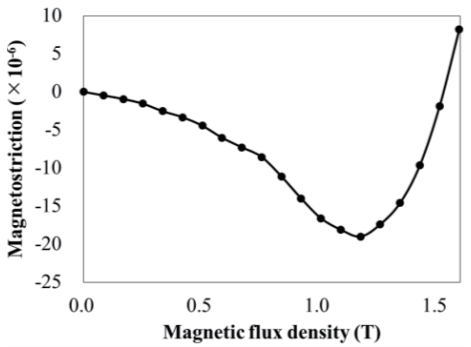

Fig. 4 Magnetic flux density versus magnetostriction characteristics.

where $\boldsymbol{p}$ is the magnetostriction force, which is expressed by the following equation when the shear force is neglected:

$$\boldsymbol{p} = \begin{bmatrix} p_x & p_y & 0 \end{bmatrix}^{\mathrm{T}} \tag{5}$$

where p_x and p_y are the x- and y-axis components of $\boldsymbol{p}$, which work in the rolling and vertical directions of each element, respectively. Here, $\boldsymbol{D}$ is the elasticity matrix expressed by the following equation.

$$\boldsymbol{D} = \frac{E}{(1+\nu)(1-2\nu)} \begin{bmatrix} 1-\nu & \nu & 0 \\ \nu & 1-\nu & 0 \\ 0 & 0 & (1-2\nu)/2 \end{bmatrix} \tag{6}$$

where E is Young's modulus and ν is Poisson's ratio, respectively. Here, E = 120 GPa and ν = 0.3, respectively. In addition, $\boldsymbol{\varepsilon}$ in the equation (4) is magnetostriction, which can be expressed by the following equation when the shear strain is neglected.

$$\boldsymbol{\varepsilon} = \begin{bmatrix} \varepsilon_x(B_x, B_y) & \varepsilon_y(B_x, B_y) & 0 \end{bmatrix}^{\mathrm{T}} \tag{7}$$

Here, the magnetostriction $\varepsilon_x(B_x, B_y)$ and $\varepsilon_y(B_x, B_y)$ generated in the x- and y-axis directions, that is the rolling and vertical directions, are expressed by the following equations, as the sum of strains generated by the magnetic flux densities B_x and B_y in the x and y axis directions, respectively.

$$\varepsilon_x(B_x, B_y) = \varepsilon_{x0}(B_x) - \nu\varepsilon_{y0}(B_y) \tag{8}$$

$$\varepsilon_y(B_x, B_y) = -\nu\varepsilon_{x0}(B_x) + \varepsilon_{y0}(B_y) \tag{9}$$

where ε_{x0} and ε_{y0} are magnetostriction corresponding to the magnetic flux densities B_x and B_y in the magnetic flux density versus magnetostriction characteristics shown in Fig. 4.

4. Simulation Results

By using the proposed method, the magnetostriction force applied to the wound core is calculated based on the magnetic flux density distribution obtained from RNA when the sine wave voltage, with the amplitude of 100 V and the frequency of 50 Hz, is applied. The validity of the proposed method is verified by comparing with the calculation results obtained from the 2-D FEM by using the JMAG-Designer Ver.18.1, which is general-purpose electro-magnetic simulation software. Fig. 5 shows the enlarged view of 2-D FEM model of the wound core, with 73,300 elements. In addition, Fig. 6 and 7 show contour maps of calculation results of magnetic flux density and magnetostriction force obtained from the FEM, respectively.

Fig. 8 shows the edges where calculation results are compared. The average magnetic flux densities of

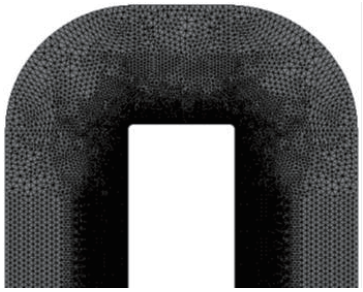

Fig. 5 Enlarged view of 2-D FEM model of a wound core.

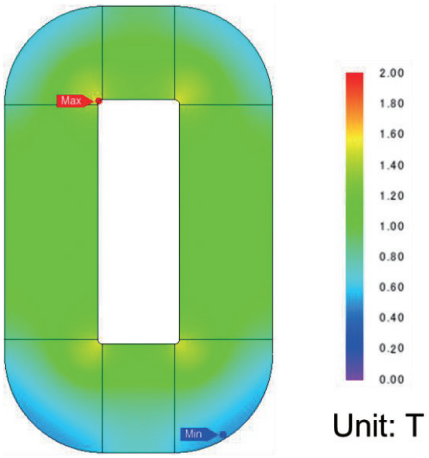

Fig. 6 Contour map of calculation result of magnetic flux density obtained from FEM.

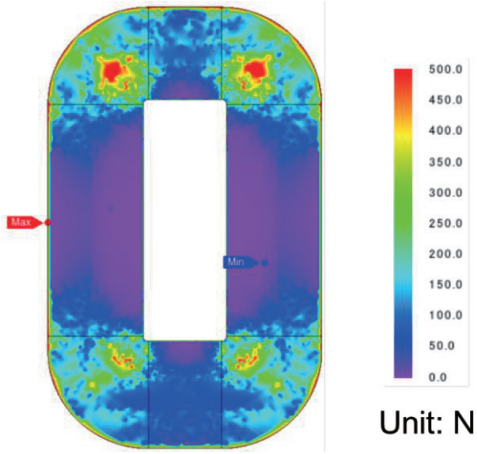

Fig. 7 Contour map of calculation result of magnetostriction force obtained from FEM.

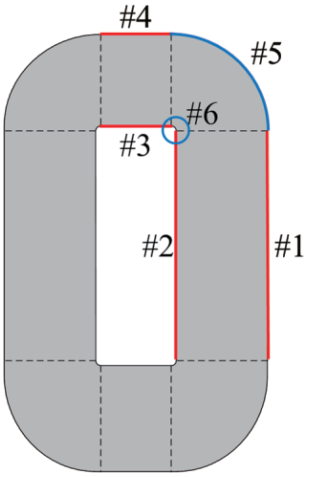

Fig. 8 Compared edges of calculation results.

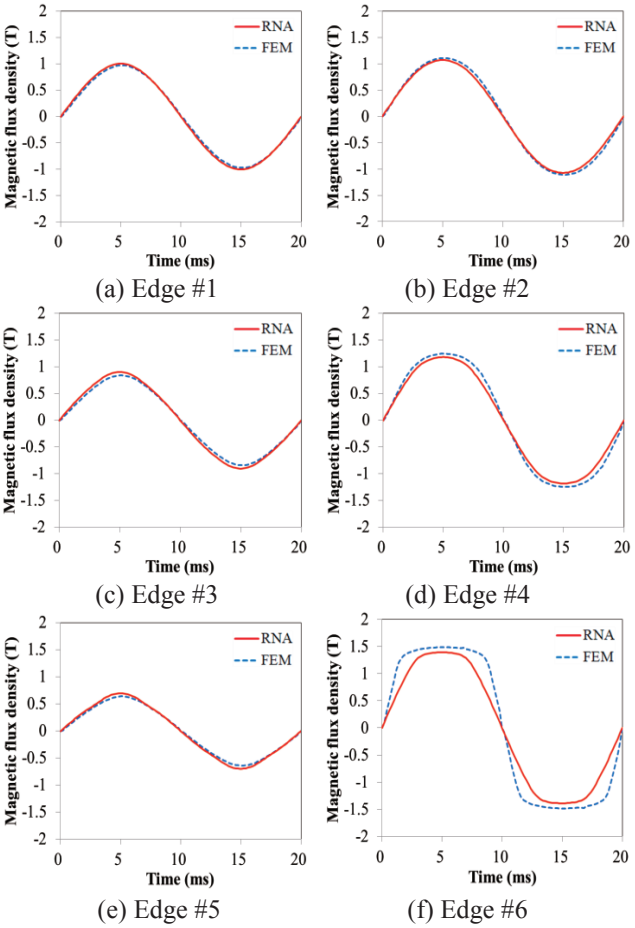

Fig. 9 Comparison of calculation results of magnetic flux density waveforms obtained from RNA and FEM.

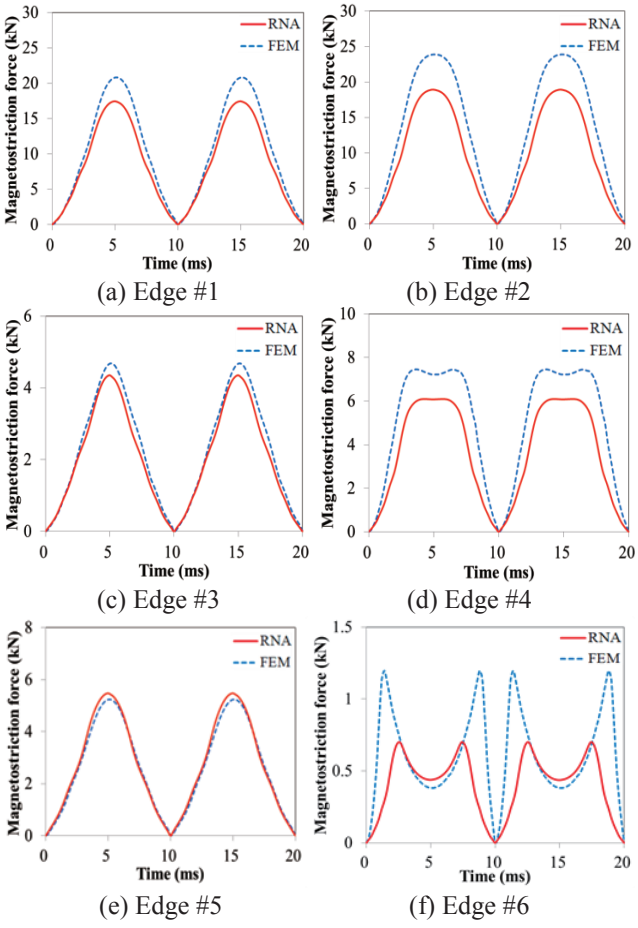

Fig. 10 Comparison of calculation results of magnetostriction force waveforms obtained from RNA and FEM.

elements adjacent to the edges #1~#6, and the magnetostriction forces applied in the direction perpendicular to the edges #1~#6 in the figure are compared between the RNA and the FEM.

Fig. 9(a)–(f) show the comparisons of calculation results of the magnetic flux density waveforms, which are obtained by taking the average value in the rolling direction in every element adjacent to each edge, for both the RNA and FEM. From these figures, it is understood that the calculated values of the RNA and FEM are in good agreement on the edges #1~#5, while there is a large error on the edge #6.

Fig. 10(a)–(f) show the comparisons of calculation results of the magnetostriction force waveforms, which are calculated by summing the forces acting perpendicular to the edges for all elements adjacent to the corresponding edge, for both the RNA and FEM. From these figures, it is clear that the calculated values of the RNA and FEM are almost in good agreement, although the errors are larger compared with those of the magnetic flux density waveforms. On the other hand, there is a large error as well as on the edge #6. It is assumed that one of the causes of these errors is the calculation accuracy of the magnetic flux density distribution due to the difference in the number of divided elements between the RNA and FEM.

Therefore, in order to verify the cause of the above errors, the magnetic flux density and magnetostriction force are calculated by using the more finely divided RNA model. Here, the core is divided into 5 by a ratio of 1:4:5:4:1 in the thickness direction, and 32 in the rolling direction, respectively. Fig. 11 shows a division of the finely divided RNA model of the wound core.

Fig. 12(a)–(f) show the comparisons of calculation results of the magnetic flux density waveforms. From these figures, it is understood that the calculated values of the RNA and FEM are in good agreement on all the edges.

Fig. 13(a)–(f) show the comparisons of calculation results of the magnetostriction force waveforms. From these figures, it is clear that the measured and calculated values are almost in good agreement on all the edges. The cause of the error seems to be that the self-made algorithm of the magnetostriction force calculation for the RNA is strictly different from JMAG algorithm.

Additionally, the calculation time is less than 1 second for the RNA whereas approximately 1 minute for the FEM, which indicates that the proposed method can significantly shorten the calculation time when the 3-D electromagnetic-structural-acoustic coupled analysis will be performed in the future.

5. Conclusion

This paper presented the calculation method for the magnetostriction force based on the RNA.
As a result, it was clear that the proposed method can calculate the magnetostriction force with relatively high accuracy and in a very short time, compared with the results of the FEM.

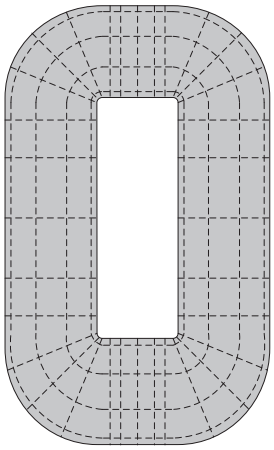

Fig. 11 Division of a finely divided RNA model of a wound core.

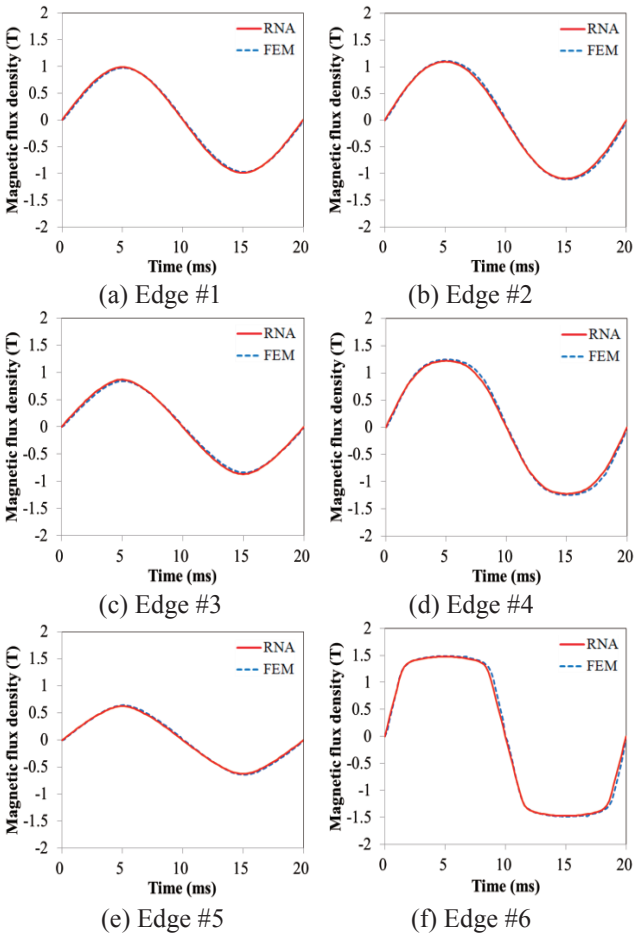

Fig. 12 Comparison of calculation results of magnetic flux density waveforms obtained from finely divided RNA and FEM.

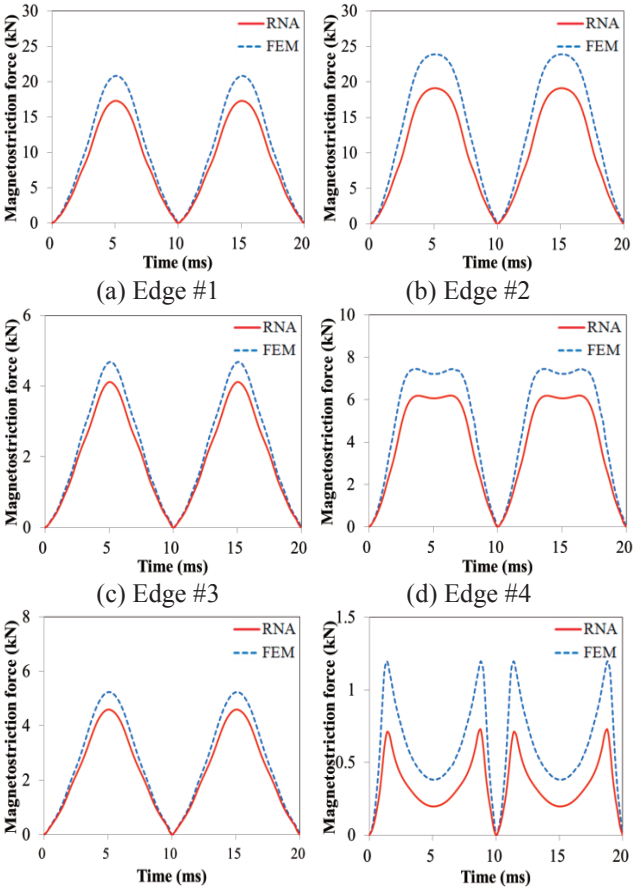

Fig. 13 Comparison of calculation results of magnetostriction force waveforms obtained from finely divided RNA and FEM.

In the future, we plan to perform structural and acoustic analysis by using the obtained magnetostriction force, and prove the validity of the proposed method experimentally.

Acknowledgements This work was supported by Grant-in Aid for JSPS Fellows (JP19J20572).

References

1) A. J. Moses, *IEEE Trans. Magn.*, **10**, 154 (1974).
2) W. Kitagawa, Y. Ishihara, T. Todaka, and A. Nakasaka, *IEEJ Trans. PE*, **128**, 654 (2008).
3) K. Nakamura and O. Ichinokura, *IEEJ Trans. FM*, **128**, 506 (2008).
4) K. Nakamura, K. Kimura, and O. Ichinokura, *Journal of Magnetism and Magnetic Materials*, **290-291**, 1309 (2005).
5) M. Fukuoka, K. Nakamura, and O. Ichinokura, *IEEE Trans. Magnetics*, **47**, 2414 (2011).
6) K. Nakamura, K. Honma, T. Ohinata, K. Arimatsu, T. Shirasaki, and O. Ichinokura, *Journal of the Magnetics Society of Japan*, **38**, 174 (2014).
7) S. Taguchi, T. Yamamoto, and A. Sakakura, *IEEE Trans. Magn.*, **10**, 123 (1974).

Received Dec. 23, 2020; Revised Feb. 2, 2021; Accepted Feb. 10, 2021

J. Magn. Soc. Jpn., **45**, 61-65 (2021)

<Paper>

Temperature difference dependence of coercivity of spin Seebeck voltage for $BiY_2Fe_5O_{12}$/Pt device made by metal organic decomposition method

Y. Takahashi, T. Takase, and K. Yamaguchi

Faculty of Symbiotic Systems Science, Fukushima Univ., *1 Kanayagawa, Fukushima-city, Fukushima 960-1296, Japan*

The temperature difference ΔT and the thickness dependences of the spin Seebeck voltage (V_{SSE}) were investigated for the polycrystalline $BiY_2Fe_5O_{12}$/Pt device made by metal organic decomposition method. As a result of investigation of the ΔT dependence of V_{SSE}, it was shown that the coercivity of V_{SSE} largely changed at the certain temperature difference ΔT_g, and ΔT_g was decreased with the thickness of $BiY_2Fe_5O_{12}$ thin film increases. When $\Delta T > \Delta T_g$, the coercivity of V_{SSE} was almost the same as the coercivity of magnetization curve for the $BiY_2Fe_5O_{12}$/Pt device. On the other hand, when $\Delta T < \Delta T_g$, the coercivity of V_{SSE} was about twice as the coercivity of V_{SSE} when $\Delta T > \Delta T_g$. Focus attention on the remanence of V_{SSE} which the gap occurs in the coercivity of V_{SSE} is almost constant independently of the thickness of $BiY_2Fe_5O_{12}$ thin films.

Key words: spin Seebeck voltage, Bi:YIG/Pt device, metal organic decomposition method, temperature difference dependence, coercivity of V_{SSE}

1. Introduction

The "spin Seebeck device" is composed of two layers which ferromagnetic material and paramagnetic metal, and utilizes spin current generated by temperature gradient at the interface of two layers[1]. The device has characteristics, where the thermoelectric output (electric power) is increased simply by expanding the area of the device [2], different from the traditional "Seebeck device".

We have made the polycrystalline $BiY_2Fe_5O_{12}$ (Bi:YIG) thin film on an inexpensive quartz glass substrate by the metal organic decomposition (MOD) method[3] which can be easily applied to expanding the area. For the purpose of improving the electromotive force converted from spin Seebeck effect (hereafter, spin Seebeck voltage: V_{SSE}), we had investigated the best annealing temperature[4].

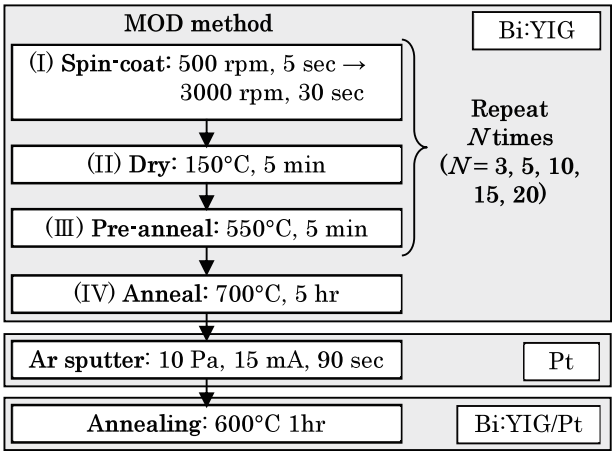

Fig. 1 Process for making Bi:YIG/Pt device samples.

Corresponding author: Yuta Takahashi
(e-mail: fa0.mtyu715.0210@gmail.com)

In this paper, we studied the temperature difference and the thickness dependences of V_{SSE} for the Bi:YIG/Pt device made based on the above method.

2. Experimental method

2.1 Making Bi:YIG/Pt device samples

Figure 1 shows the process for making Bi:YIG/Pt device samples. The substrate was used quartz glass with a length=13 mm, a width=7 mm, and a thickness= 0.45 mm. The Bi:YIG thin film was made by four steps as following: "(I) Spin Coat" of MOD solution on the substrate, "(II) Dry" to remove organic solvent, "(Ⅲ) Pre-anneal" to decompose organometallic compounds and make them precursors of metal oxides, "(IV) Anneal" for crystallization. Here, the steps of "Spin Coat", "Dry", and "Pre-anneal" were repeated N times (N = 3, 5, 10, 15, and 20) to change the thickness of the Bi:YIG thin film. Next, Pt thin film was formed by sputtering over the surface area of Bi:YIG thin film. In order to estimate the thickness of Bi:YIG thin film and Pt thin film, the cross

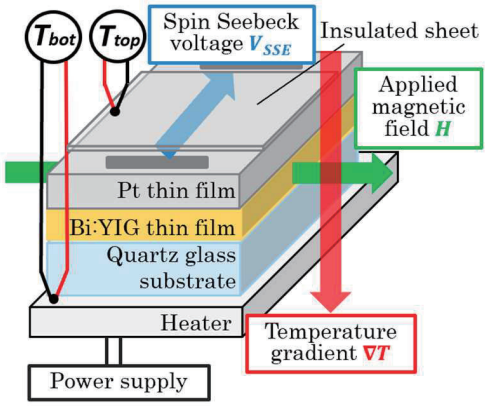

Fig. 2 Experimental configuration of measuring V_{SSE}, T_{top} and T_{Bot} for Bi:YIG/Pt device samples.

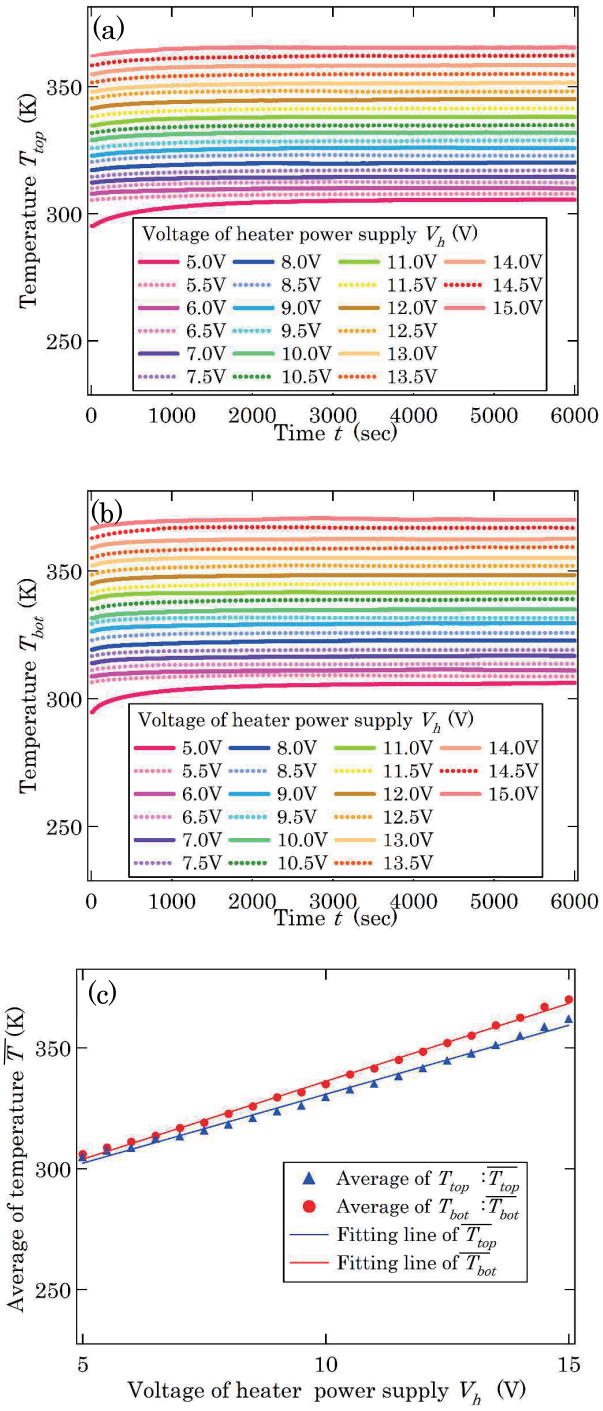

Fig. 3 The time dependences of (a) T_{top} and (b) T_{bot} at each V_h in the sample (N=20) (c) The average of T_{top} and T_{bot} as a function of the V_h, and fitting line of $\overline{T_{top}}$ and $\overline{T_{bot}}$.

section for the sample (N= 10) was observed by SEM. As a result, it was observed that the Bi:YIG thin film when N= 10 was about 400 nm and the Pt thin film was about 10 nm. Finally, glass/Bi:YIG/Pt was annealed at 600 °C for 1 hour in an air atmosphere. For details on the process for making Bi:YIG/Pt device samples, refer to Ref 4).

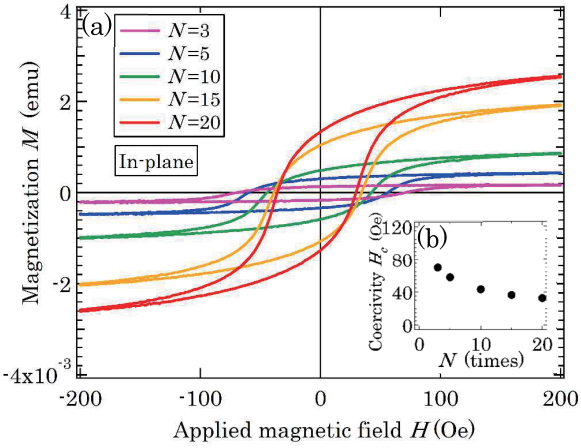

Fig. 4 (a)M-H curves for each sample (N=3, 5, 10, 15, and 20) by VSM. (b)The coercivity H_c of M-H curves as a function of the N.

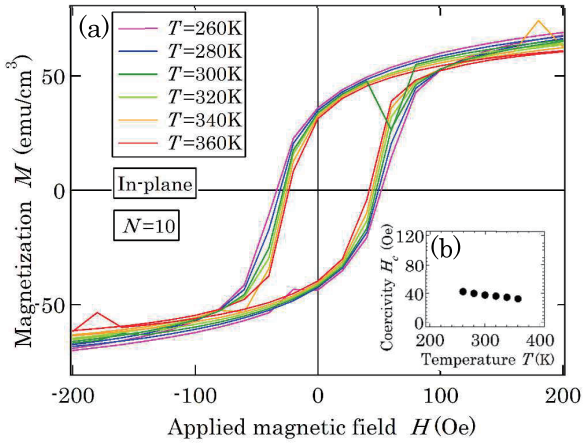

Fig. 5 (a)T dependences of M-H curves for the sample (N=10) by SQUID magnetometer. (b)The coercivity H_c of M-H curves as a function of the T.

2.2 Measurements of the magnetization and the V_{SSE} for Bi:YIG/Pt device samples

The Applied magnetic field H dependences of the magnetization M (M-H curves) for Bi:YIG/Pt device samples were measured by using vibrating sample magnetometer (VSM, Tamagawa Seisakujo; type TM-VSM1015) at room temperature. The absolute temperature dependences of M-H curves for Bi:YIG/Pt device samples were measured by using superconducting quantum interference device magnetometer (SQUID magnetometer, Quantum Design; MPMS). In both measurements, H was in the in-plane direction of the sample.

Figure 2 shows experimental configuration of measuring V_{SSE} for Bi:YIG/Pt device samples. When H was in the in-plane direction of the sample and the temperature gradient ∇T generated in the perpendicular direction of the sample, and electric potential difference between the electrodes of the sample perpendicular to each was measured as the V_{SSE}. The H was swept from -200 Oe to

200 Oe.

2.3 Measurement of the temperature of top and bottom of surfaces for Bi:YIG/Pt device samples

The temperature gradient was generated by the small ceramic heater (MISUMI; MMCPH) placed under the sample (bottom side). Temperature difference between top and bottom of surfaces ΔT was controlled by voltage of the power supply V_h applied to the heater. The stabilization of the temperature of top and bottom of surfaces of the sample, T_{top} and T_{bot} were confirmed, before measuring the ΔT dependence of the V_{SSE} shown in Sec. 2.2. Figure 2 shows the experimental configuration of measuring the T_{top} and T_{bot} for Bi:YIG/Pt device samples. The T_{top} and T_{bot} were each measured by two K-type thermocouples, after running the heater. The time dependences of T_{top} and T_{bot} at each V_h for the sample (N =20) are shown in Fig. 3(a) and (b), respectively. These can be shown, that was stable after 3000 sec, therefore, the average values from 4000 sec to 6000 sec as a function of the V_h are shown in Fig. 3(c), as $\overline{T_{top}}$, and $\overline{T_{bot}}$. Two solid lines are an approximate straight line to which the least squares method was used. The difference between these approximate straight lines is used as a conversion equation for V_h and the ΔT, as below

$$\Delta T(\mathrm{K}) = 0.73V_h - 2.0 \qquad (1).$$

The same measurement was performed for each sample (N= 3, 5, 10, and 15), and it was checked that Eq. (1) can be applied to these samples too. In this paper, the V_h is in the range of 5.0V to 15.0V (ΔT is from 1.7K to 9.0K, applying Eq. (1)), and the V_{SSE} was measured with increasing ΔT.

3. Experimental results

3.1 The thickness and the absolute temperature dependences of M-H curves

The magnetic characteristics of the Bi:YIG/Pt device samples were investigated, before measuring the V_{SSE}.

Figure 4(a) shows the M-H curves for each sample (N = 3, 5, 10, 15, and 20) by using VSM. It was illustrated that the M increased with increasing the N, each M was 1.9×10^{-4}, 4.5×10^{-4}, 9.3×10^{-4}, 2.0×10^{-3}, and 2.6×10^{-3} emu when H =200 Oe. Figure 4(b) shows the coercivity H_c of M-H curves as a function of the N. It was illustrated that the H_c decreased with increasing the N. The thickness of Bi:YIG thin film experimentally was estimated for each sample (N= 3, 5, 15, and 20), based on the thickness of the Bi:YIG thin film (about 400 nm) and the M (9.3×10^{-4}

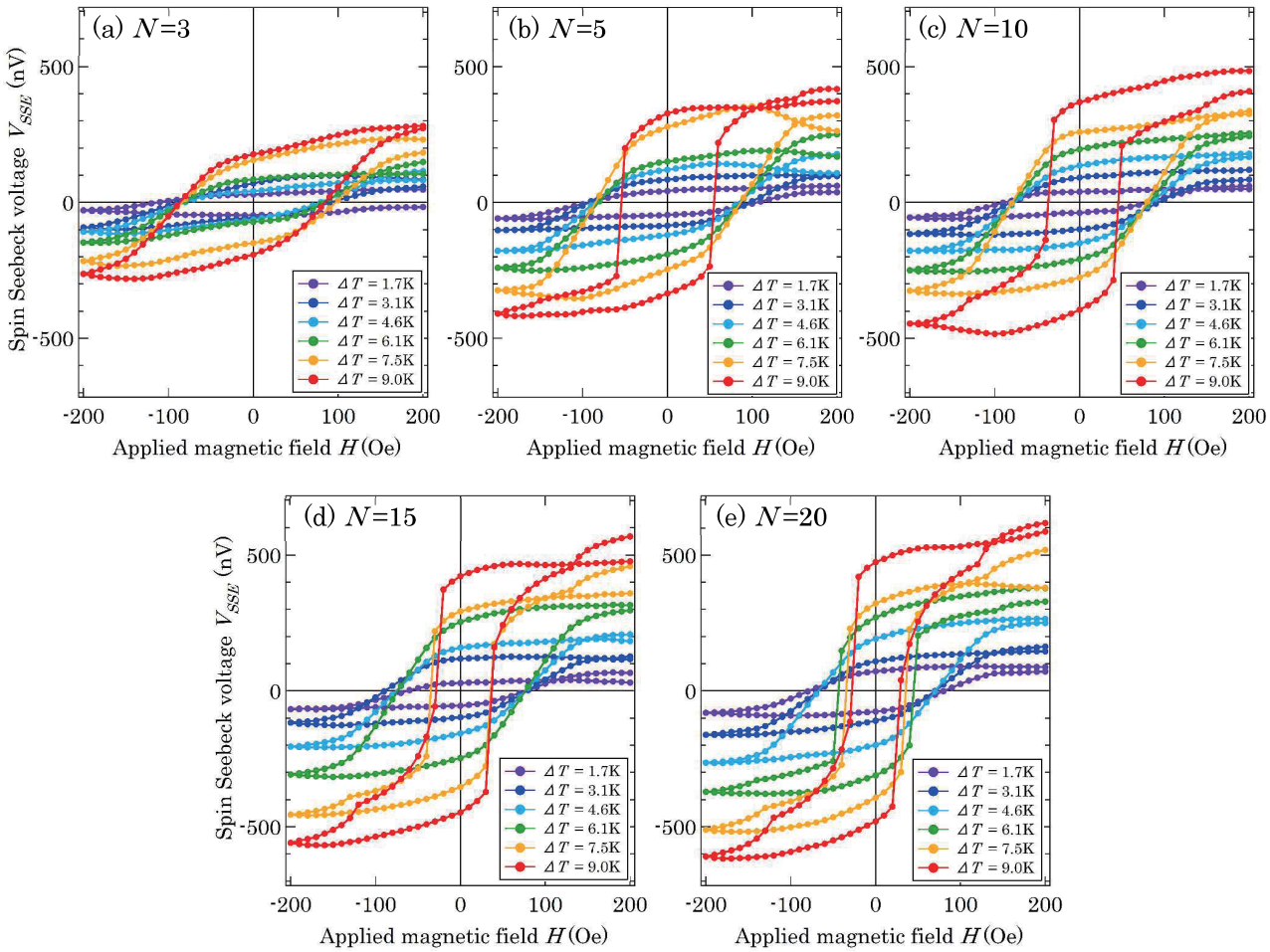

Fig. 6 The V_{SSE} as a function of the H for ΔT=1.7, 3.1, 4.6, 6.1, 7.5, 9.0K for each sample ((a) N=3, (b) N=5, (c) N=10, (d) N=15, and (e) N=20).

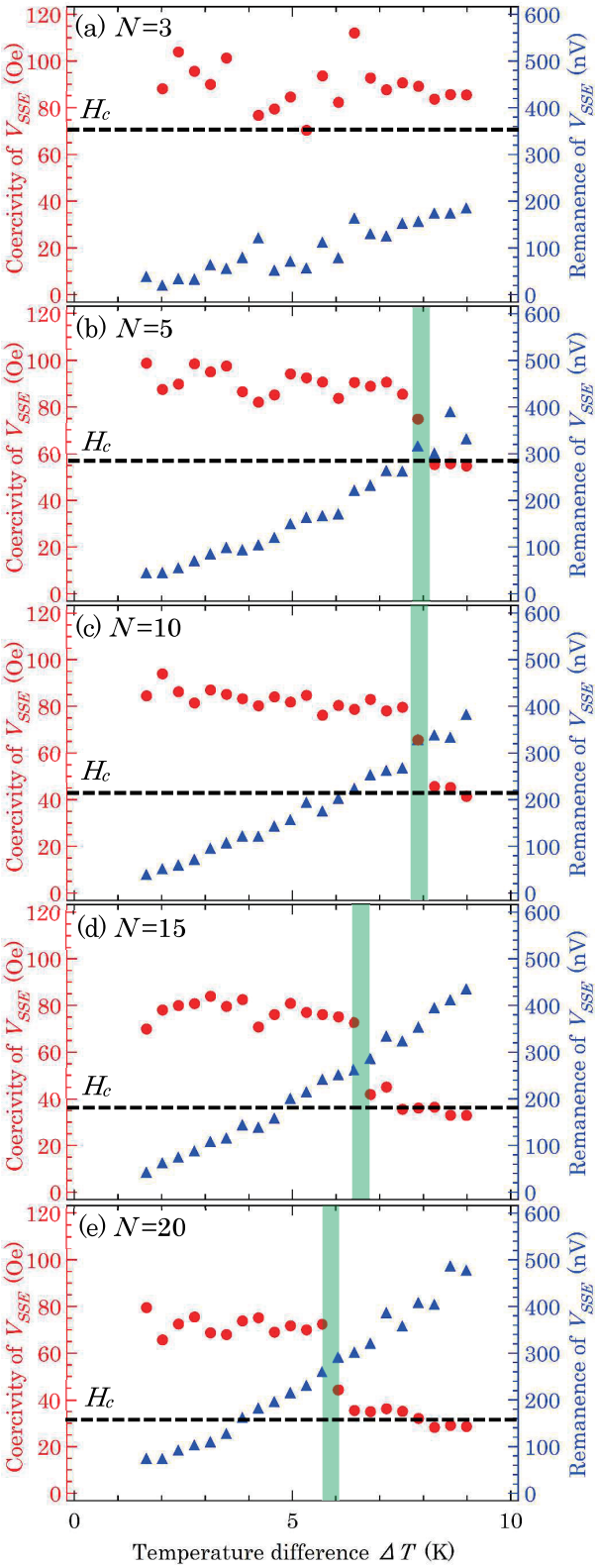

Fig. 7 ΔT dependence of the coercivity of V_{SSE} and the remanence of V_{SSE} for each sample ((a) N=3, (b) N=5, (c) N=10, (d) N=15, and (e) N=20). H_c of M-H curve for each sample shown in Fig. 4 (b) are added with black dashed lines as to correspond to the scale of left vertical axis.

emu) of the sample (N=10). As a result, each thickness of Bi:YIG thin film was estimated at about 80, 190, 850, and 1100 nm, respectively.

Figure 5(a) shows the absolute temperature T dependence of M-H curves for the sample (N=10) by using SQUID magnetometer in the range of 260K to 360K. Here, the M is normalized per unit volume of the Bi:YIG thin film. Figure 5(b) shows the coercivity H_c of M-H curves as a function of the T. Figure 5(a) and (b) were illustrated the both M and H_c were changed no significant in the absolute temperature range in this measurement.

3.2 ΔT dependence of the V_{SSE}

ΔT dependence of the V_{SSE} was measured for each sample (N = 3, 5, 10, 15, and 20) with increasing ΔT. Figure 6 shows the V_{SSE} as a function of the H for ΔT=1.7, 3.1, 4.6, 6.1, 7.5, 9.0K. Here, the V_{SSE} when the H becomes zero is defined to the "remanence of V_{SSE}", and the H when the V_{SSE} becomes zero is defined to the "coercivity of V_{SSE}". It was illustrated that the remanence of V_{SSE} increases with increasing ΔT in the same sample, and also increase with increasing the N in the same ΔT. In the point of view of coercivity of V_{SSE}, it largely changed at the certain ΔT, except for the sample (N=3).

4. Discussion

Based on the above results, behaviors of the coercivity of V_{SSE} for the Bi:YIG/Pt device samples were discussed. Figures 7(a) to 7(e) show the ΔT dependence of the coercivity of the V_{SSE} and the remanence of V_{SSE} for each sample, in addition to the ΔT except for it shown in Fig. 6. From Fig. 7(a) to (e), it was shown that the coercivity of V_{SSE} largely changes in at the certain ΔT shown in the green region, except for the sample (N=3). Here, the ΔT shown in the green region is defined to "ΔT_g", because it is the ΔT which the gap occurs in the coercivity of V_{SSE}. As shown in Fig. 7 (a) to (e), ΔT_g was decreased with the N increases. The H_c for each sample shown in Fig. 4 (b) is added with black dashed lines in Fig. 7(a) to (e), so as to correspond to the scale of left vertical axis. In this shown, when $\Delta T > \Delta T_g$, the coercivity of V_{SSE} was almost the same as the H_c for each sample. On the other hand, when $\Delta T < \Delta T_g$, the coercivity of V_{SSE} was about twice as the coercivity of V_{SSE} when $\Delta T > \Delta T_g$.

Figure 8 shows the coercivity of V_{SSE} as a function of the remanence of V_{SSE} for each sample. As mentioned above, it was shown that the ΔT depends on the N, however, it was shown that the remanence of V_{SSE} which the gap occurs in the coercivity of V_{SSE} is almost constant at about 290nV independently of the N. It is suggested that the large change in the coercivity of V_{SSE} may be due to the amount of spin current.

It is well known that the coercivity of V_{SSE} changes in samples which have different surface roughness of the ferromagnetic material, because the V_{SSE} reflects the magnetization information only near the interface[5,6]. In this paper, however, it is suggested that the large change

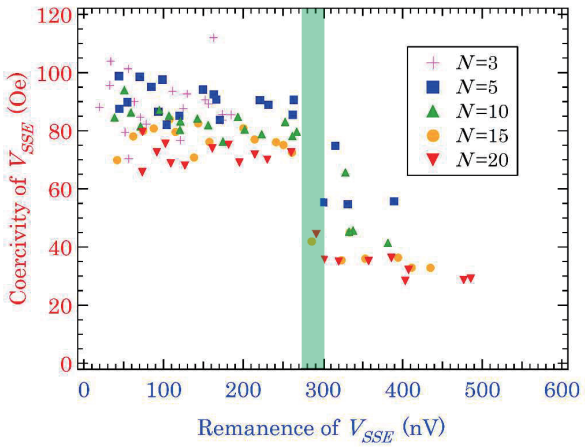

Fig. 8 The coercivity of V_{SSE} as a function of the remanence of V_{SSE} for each sample.

of the coercivity of V_{SSE} in the same sample by only ΔT is difference result, compared to above behavior depending on the surface roughness.

5. Conclusion

As a result of investigation of the temperature difference dependence of the spin Seebeck voltage (V_{SSE}) for the polycrystalline $BiY_2Fe_5O_{12}$ (Bi:YIG)/Pt device, it was shown that the coercivity of V_{SSE} largely changed at the certain temperature difference ΔT_g, and ΔT_g was decreased with the thickness of the Bi:YIG thin film increases. Focus attention on the remanence of V_{SSE} which the gap occurs in the coercivity of the V_{SSE} is almost constant independently of the thickness of Bi:YIG thin films. It is suggested that the large change in the coercivity of V_{SSE} may be due to the amount of spin current.

Experimental studies of the spin Seebeck effect have mainly focused on improving magnitude of V_{SSE} per unit temperature difference and searching for new materials, and haven't been paid attention to the coercivity of V_{SSE}.

In this measurement, it is suggested that there is a discontinuous point in the coercivity of V_{SSE} which indicates that the direction of spin is hard to reverse in the spin current. The unique behavior of coercivity of V_{SSE} may be peculiar to polycrystalline Bi:YIG/Pt devices made by the metal organic decomposition method. In the future, it will be necessary to systematically investigation the process of the hysteresis loop of V_{SSE} at the spin Seebeck device based on polycrystalline ferromagnetic thin film to reveal the origin of this behavior.

References

1) K. Uchida, H. Adachi, T. Kikkawa, A. Kirihara, M. Ishida, S. Yorozu, S. Maekawa, and E. Saitoh: *Proc. IEEE*, **104**, 1946-1973 (2016).
2) A. Kirihara, K. Uchida, Y. Kajiwara, M. Ishida, Y. Nakamura, T. Manako, E. Saitoh, and S. Yorozu: *Nature Materials*, **11**, 686-689 (2012).
3) T. Ishibashi, A. Mizusawa, M. Nagai, S. Shimizu, and K. Sato: *J. Appl. Phys.*, **97**, 013516 (2005).
4) Y. Takahashi, T. Takase, and K. Yamaguchi: *T. Magn. Soc. Jpn. (Special Issues).*, **4**, 14-17(2020) [in Japanese].
5) A. Aqeel, I. J. Vera-Marun, B. J. van Wees, and T. T. M. Palstra: *J. Appl. Phys.*, **116**, 153705 (2014).
6) K. Uchida, J. Ohe, T. Kikkawa, S. Daimon, D. Hou, Z. Qui, and E. Saitoh: *Phys. Rev. B*, **92**, 014415 (2015).

Received Dec. 30, 2020; Accepted Feb. 12, 2021

J. Magn. Soc. Jpn., **45**, 66-69 (2021)

<Paper>

Structure and magnetic properties of $Sm(Fe_{0.8}Co_{0.2})_{12}$ thin films by adding light elements

M. Kambayashi[*], H. Kato[**], Y. Mori[**], M. Doi[*, ***] and T. Shima[*, ***]

[*] Graduate School of Engineering, Tohoku Gakuin Univ., *1-13-1 Tagajo 985-8537 Japan*

[**] Department of Engineering, Tohoku Gakuin Univ., *1-13-1 Tagajo 985-8537 Japan*

[***] Elements Strategy Initiative Center for Magnetic Materials (ESICMM), National Institute for Materials Science, *1-2-1 Sengen Tsukuba 305-0047, Japan*

The effect of light elements such as B, C and N on $Sm(Fe_{0.8}Co_{0.2})_{12}$ alloy was investigated in detail. The highest coercivity H_c of 11.1 kOe was obtained for $Sm(Fe_{0.8}Co_{0.2})_{12}$-B thin films with the thickness of 100 nm and B content of 11.2 at.%. From X-ray diffraction patterns, peaks from (002) and (004) of $ThMn_{12}$-type phase were clearly observed for the films. However, no significant improvement in magnetic properties was observed with the addition of C and N to the $Sm(Fe_{0.8}Co_{0.2})_{12}$ alloy, as was the case with the combined addition with B. It was confirmed that only the addition of B contributes significantly to the improvement of magnetic properties from the result of adding light elements to this series of $Sm(Fe_{0.8}Co_{0.2})_{12}$ alloy.

Keywords: RFe_{12} compound, $ThMn_{12}$-type structure, $Sm(Fe_{0.8}Co_{0.2})_{12}$ alloy, light elements, coercivity

1. Introduction

RFe_{12} (R: rare-earth elements) compounds[1)-3)] with a tetragonal $ThMn_{12}$-type crystal structure are expected to surpass the magnetic properties of Nd-Fe-B sintered magnets, since RFe_{12} compounds possess high saturation magnetization M_s and high anisotropy field H_A by the largest composition ratio 1:12 of R atom versus Fe atoms which have high molar fraction among $R_{m-n}Fe_{5m+2}$ systems. However, the RFe_{12} compounds are known to be very unstable from a thermodynamic point of view, and it has been realized that the RFe_{12} phase have been successfully stabilized only by substitution of the element M (M = Cr, V, Ti, Mo, W, Si and Fe)[4)-7)]. Unfortunately, the substitution of Fe with a large amount of M causes a reduction in saturation magnetization M_s. Therefore, there is a strong demand for the realization of $R(Fe, M)_{12}$ compounds having high phase stability by substituting a small amount of elements.

In recent years, Hirayama et al. reported that the $Sm(Fe_{0.8}Co_{0.2})_{12}$ thin films with a film thickness of 595 nm deposited on a MgO (100) single crystal substrate with V underlayer grow epitaxially, and their representative magnetic properties of M_s of 1.78 T, anisotropy field H_A of 120 kOe and Curie temperature T_C of 586 ºC, which surpasses that of $Nd_2Fe_{14}B$ compound. Since then, a lot of studies have been performed on $Sm(Fe_{0.8}Co_{0.2})_{12}$ compound with changing the fabrication conditions[8)-10)]. Previously, we have successfully reported that the large coercivity of 1.2 T can be achieved by the addition of B to an anisotropic $Sm(Fe_{0.8}Co_{0.2})_{12}$ thin film[11)]. It is thought that additive elements will play an important role for improving the magnetic properties of the $Sm(Fe_{0.8}Co_{0.2})_{12}$ compounds.

Since the light elements B, C and N have small atomic radii, they are expected to be alloyed by interstitial or substitutional position in the $ThMn_{12}$-type main phase or grain boundary phase and it is considered to have a great influence on the structure and magnetic properties of $Sm(Fe_{0.8}Co_{0.2})_{12}$ compound. The effect of light elements on this compound has not been fully studied yet, although the effect of N addition for R-Fe compounds have been widely investigated[12)]. In this study, in order to see the effect of light elements on the structure and magnetic properties for $Sm(Fe_{0.8}Co_{0.2})_{12}$ thin films, $Sm(Fe_{0.8}Co_{0.2})_{12}$-$X$ (X = B, C, N, B-C and B-N) have been fabricated and their structure and magnetic properties have also been investigated.

2. Experimental procedure

The samples were prepared by using ultra-high vacuum magnetron sputtering system with base pressure of less than 1.0×10^{-8} Pa. First of all, a V underlayer of 20 nm was deposited onto the MgO (100) single crystal substrate at substrate temperature T_s of 350 ºC. Then, the $Sm(Fe_{0.8}Co_{0.2})_{12}$-$X$ (X = B, C, N, B-C and B-N) layer was deposited. Film thickness of $Sm(Fe_{0.8}Co_{0.2})_{12}$-B thin films was changed from 5 to 200 nm, while it was fixed to 100 nm for another samples with C or N addition. The composition of B and C was designed and calculated by the deposition rate of co-deposition of the targets. On the other hand, the amount of N addition was adjusted by the ratio of Ar gas and N_2 gas during deposition. Highly accurate elemental analysis of light element is not easy, however, B content has been analyzed by inductively coupled plasma (ICP) spectroscopy to be $Sm_{7.3}Fe_{67.6}Co_{16.0}B_{9.1}$

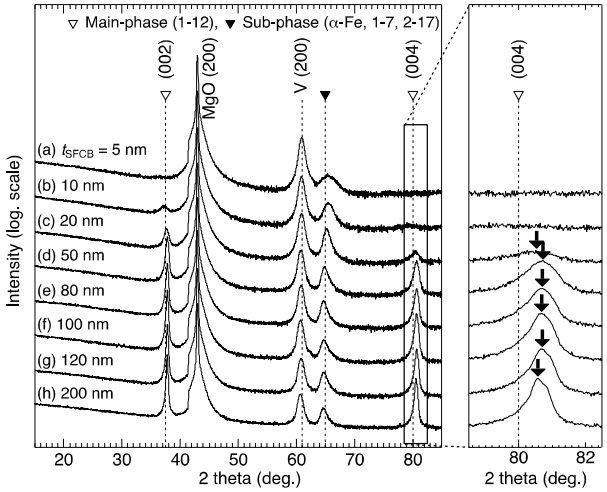

Fig. 1. Effect of film thickness on the XRD patterns for $Sm(Fe_{0.8}Co_{0.2})_{12}$-B thin films. The film thickness t_{SFCB} was changed from 5 to 200 nm. Enlarged view of the high-angle (004) peak is also shown.

Corresponding author: T. Shima
(e-mail: shima@mail.tohoku-gakuin.ac.jp).

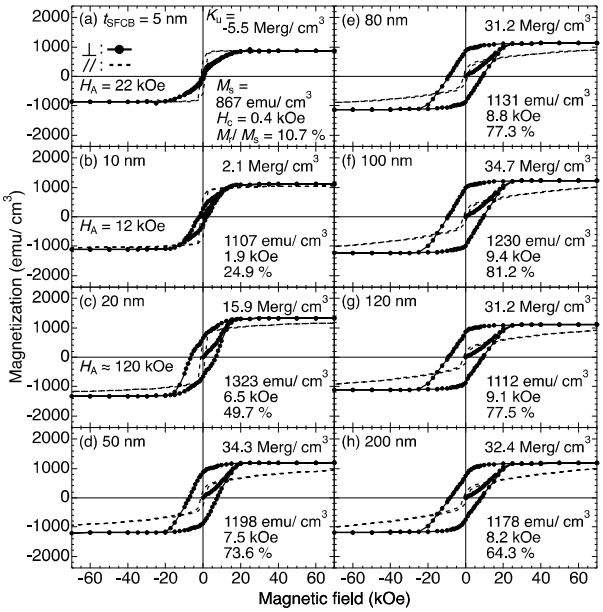

Fig. 2. Effect of film thickness on the *M-H* curves for Sm(Fe$_{0.8}$Co$_{0.2}$)$_{12}$-B thin films measured in applied field perpendicular (solid line) and parallel (dotted line) to the film plane. The film thickness t_{SFCB} was changed from 5 to 200 nm.

(at.%) for the film with B = 9.1 at.% was determined in a previous report[11]. Although the exact amount of C and N addition is uncertain at this moment, it was confirmed that the tendency can be understood because the amount of addition is continuously changed. The amount of B was changed from 0 to 11.3 at.%, the addition of C was designed by the deposition rate of each target and it was changed from 0 to 4.0 %, while for the addition of N, the flow rate ratio of N_2 gas to Ar gas was changed from 0 to 1.0 %. According to an energy dispersive X-ray spectroscopy (EDX) analysis, 14 at.% N was determined to the film with a flow rate ratio of N of 0.5 %, and it was about 22 at.% N to that of 1.0 %. It was confirmed that the amount of nitrogen became constant when the flow rate exceeded that. Accurate elemental analysis of C and N will be performed later. Finally, the V layer of 10 nm was deposited as a cap layer for the prevention of oxidation. The structural analysis was performed by the XRD with Cu-Kα radiation from the out-of-plane configuration, the magnetization curves were measured by using a superconducting quantum interference device (SUQID) magnetometer, the film composition was determined by EDX, and in some cases an ICP spectroscopy analysis and APFIM was performed. All measurements were performed at room temperature.

3. Results and discussion

In order to investigate the effect of film thickness on the structure and magnetic properties for Sm(Fe$_{0.8}$Co$_{0.2}$)$_{12}$-B thin films, Sm(Fe$_{0.8}$Co$_{0.2}$)$_{12}$ thin films with B content of 9.1 at.% were prepared. XRD patterns of Sm(Fe$_{0.8}$Co$_{0.2}$)$_{12}$-B thin films with different film thickness are shown in Fig. 1. The enlarged view of high-angle (004) peak was also shown. The peaks from (002) and (004) of ThMn$_{12}$-type phase with the strongly texture toward (00*l*) direction were began to observe for the film with t_{SFCB} of 20 nm and they shifted to higher angle, indicating that *c*-axis shrank. Further increasing the film thickness, the intensity of these peaks increased and the position of the peak hardly changed up to 120

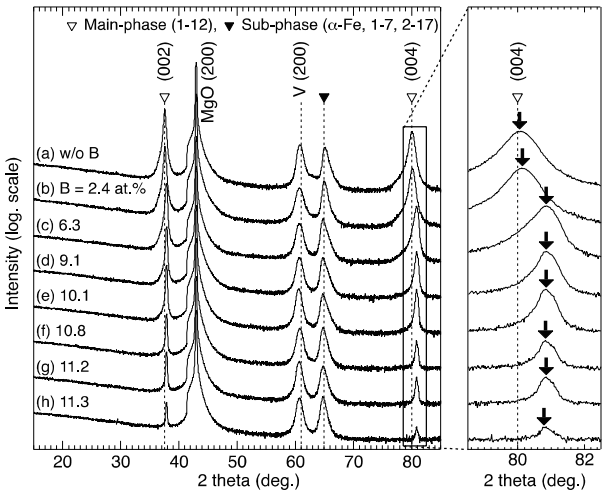

Fig. 3. XRD patterns for Sm(Fe$_{0.8}$Co$_{0.2}$)$_{12}$-B (100 nm) thin films with different B content of 0 to 11.3 at.%. Enlarged view of the high-angle (004) peak is also shown.

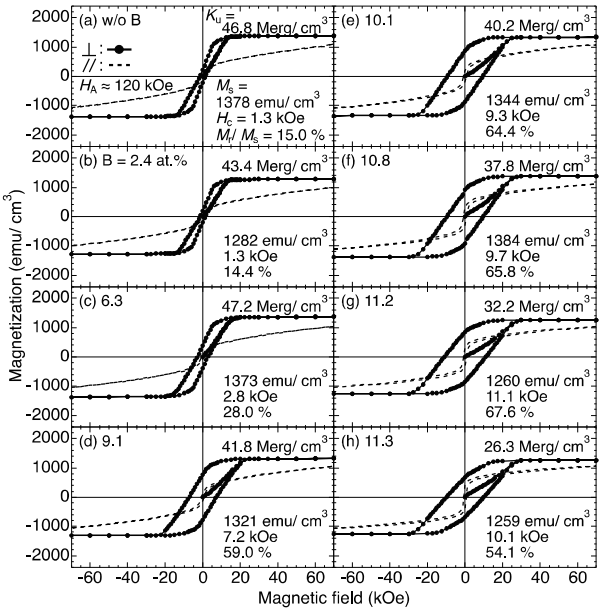

Fig. 4. *M-H* curves for Sm(Fe$_{0.8}$Co$_{0.2}$)$_{12}$-B (100 nm) thin films with different B content of 0 to 11.3 at.%.

nm, but changed to a low angle beyond that.

The magnetization curves for Sm(Fe$_{0.8}$Co$_{0.2}$)$_{12}$-B thin films with different film thickness are shown in Fig. 2. The solid and dotted lines denote the curve measured in applied field perpendicular and parallel to the film plane, respectively. It was confirmed that the H_c was increased with increasing the film thickness, and high H_c of 9.4 kOe, high M_s of 1230 emu/ cm^3 and moderate high uniaxial magnetic anisotropy K_u of 34.7 Merg/ cm^3 were obtained for the film with t_{SFCB} of 100 nm (f). With further increasing of film thickness, H_c was slightly decreased to 8.2 kOe for the film with t_{SFCB} of 200 nm (h).

Subsequently, the effect of B content to Sm(Fe$_{0.8}$Co$_{0.2}$)$_{12}$-B thin films with the film thickness of 100 nm was investigated. The XRD patterns and their enlarged view of the high-angle (004) peak for Sm(Fe$_{0.8}$Co$_{0.2}$)$_{12}$-B (100 nm) thin films are shown in Fig. 3. The peaks from (002) and (004) of ThMn$_{12}$-type compound can be observed for all the samples. With increasing B content, the intensity of these peaks decreased and shifted to higher angle for

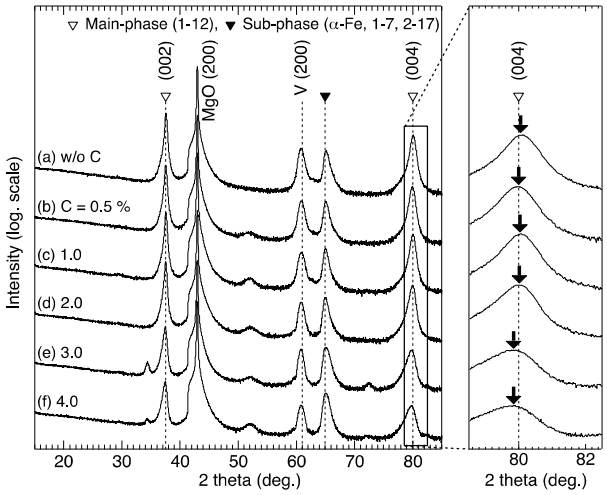

Fig. 5. XRD patterns for $Sm(Fe_{0.8}Co_{0.2})_{12}$-C (100 nm) thin films with different C content of 0 to 4.0 %. Enlarged view of the high-angle (004) peak is also shown.

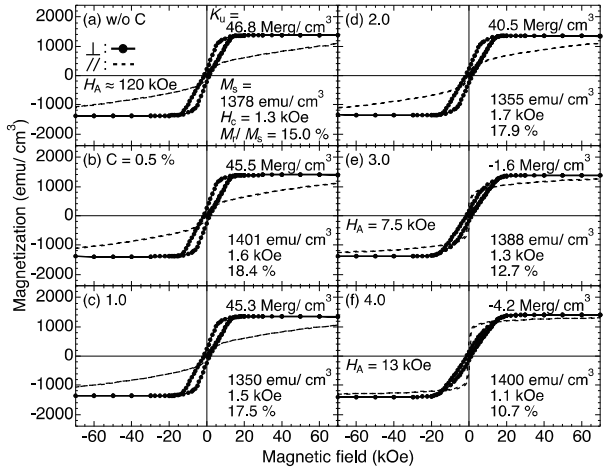

Fig. 6. *M-H* curves for $Sm(Fe_{0.8}Co_{0.2})_{12}$-C (100 nm) thin films with different C content of 0 to 4.0 %.

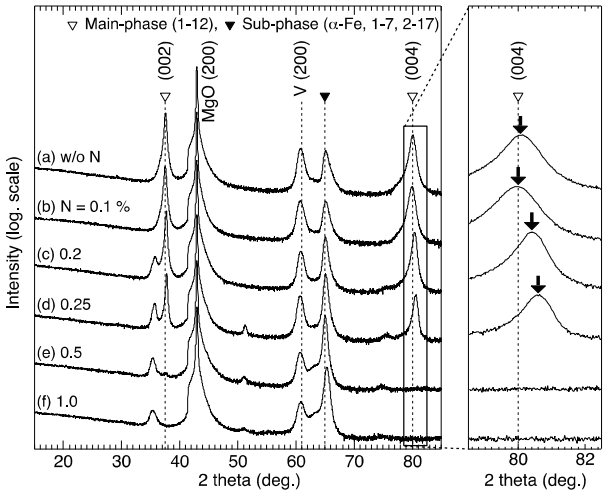

Fig. 7. XRD patterns for $Sm(Fe_{0.8}Co_{0.2})_{12}$-N (100 nm) thin films with different N content of 0 to 1.0 %. Enlarged view of the high-angle (004) peak is also shown.

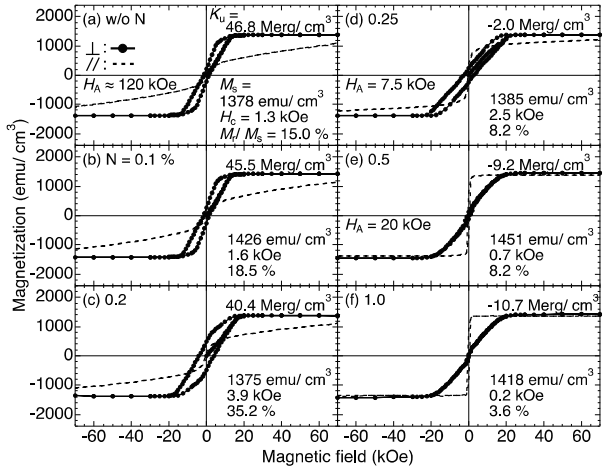

Fig. 8. *M-H* curves for $Sm(Fe_{0.8}Co_{0.2})_{12}$-N (100 nm) thin films with different N content of 0 to 1.0 %.

the film with B of 6.3 at.% (c), indicating that the lattice constant of *c*-axis slightly shrank. Also, the peaks from (004) became sharper as the amount of B increased. It is considered that this is because a columnar structure having an average grain size of about 40 nm was formed[11].

The magnetization curves for $Sm(Fe_{0.8}Co_{0.2})_{12}$-B (100 nm) thin films with different B content are shown in Fig. 4. Without B addition, low H_c of 1.3 kOe was obtained for the $Sm(Fe_{0.8}Co_{0.2})_{12}$ thin film. However, it was confirmed that the H_c was increased with increasing B content and high H_c of 11.1 kOe, high M_s of 1260 emu/ cm^3 and moderate high K_u of 32.2 Merg/ cm^3 were obtained for the film with B of 11.2 at.% (g). By a slightly increase of B content, H_c was decreased to 10.1 kOe for the film with B of 11.3 at.% (h).

XRD patterns and their enlarged view of the high-angle (004) peak for $Sm(Fe_{0.8}Co_{0.2})_{12}$-C (100 nm) thin films with different C content of 0 to 4.0 % are shown in Fig. 5. The peaks from (002) and (004) of $ThMn_{12}$-type compound were observed for all the samples. With increasing C content, the intensity of these peaks decreased and the position was almost unchanged up to C = 2.0 % (d), and shifted to lower angle when it reached 3.0 or higher, indicating that the lattice constant of *c*-axis was slightly increased for the film with C = 3.0 % (e). At 3.0 % or higher C content, $SmFe_2$ (220) and (440) peaks and $ThMn_{12}$-type superlattice (132) peaks began to observe at 34.5°, 72.1° and 52.0°.

The magnetization curves for $Sm(Fe_{0.8}Co_{0.2})_{12}$-C (100 nm) thin films with different C content are shown in Fig. 6. The out-of-plane magnetic anisotropy and low H_c was obtained for the $Sm(Fe_{0.8}Co_{0.2})_{12}$-C thin film. It was confirmed that the H_c was slightly increased with increasing C content, however, with further increasing C content to 3.0 %, H_c was decreased and magnetic anisotropy was changed from the out-of-plane to the in-plane anisotropy.

XRD patterns and their enlarged view of the high-angle (004) peak of $ThMn_{12}$-type compound for $Sm(Fe_{0.8}Co_{0.2})_{12}$-N (100 nm) thin films with different N content of 0 to 1.0 % are shown in Fig. 7. The peaks from (002) and (004) of $ThMn_{12}$-type compound were observed for the films with N content up to 0.25 %. With increasing N content as in the case of the $Sm(Fe_{0.8}Co_{0.2})_{12}$-B thin films, the intensity of these peaks decreased and shifted to higher angle, indicating the lattice constant of *c*-axis slightly shrank. It is also thought that peaks from the SmN (200) and (400) began to observe at 35.6° and 74.8° when N content was reached 0.2 % or higher, and the SmN (220) peak began to observe at 51.2° when it reached 0.25 % or higher. On the contrary to the results from B added films, C and N added samples are seemed to be almost

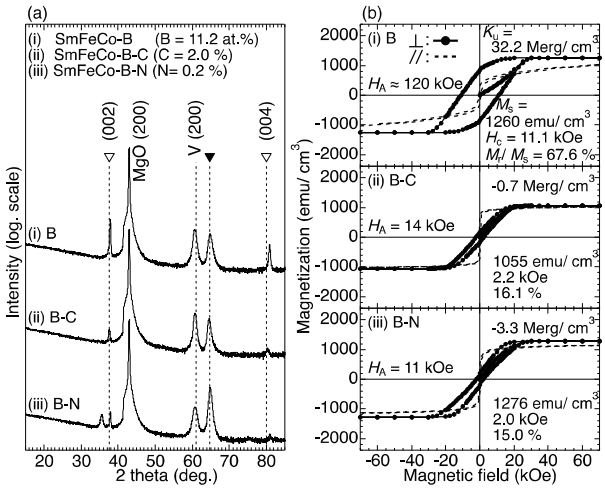

Fig. 9. XRD patterns and *M-H* curves for $Sm(Fe_{0.8}Co_{0.2})_{12}$-B (100 nm) thin films by adding C to 2.0 % and N to 0.2 %.

same width of the (004) peak, this is because the $ThMn_{12}$-type structure has hardly changed.

The magnetization curves for $Sm(Fe_{0.8}Co_{0.2})_{12}$-N (100 nm) thin films with different N content are shown in Fig. 8. It was confirmed that the H_c was slightly increased with increasing N content, and high H_c of 3.9 kOe was obtained for the film with N of 0.2 % (c). However, H_c was decreased and magnetic anisotropy was changed from the out-of-plane to the in-plane anisotropy for the film with N of 0.25 % (d). Furthermore, H_c decreased at the film with N of 0.5 % (e).

From the detail microstructural observation by 3D atom probe, the addition of B to the $Sm(Fe_{0.8}Co_{0.2})_{12}$ film leads to the formation of amorphous intergranular phase and B rich shell can be observed in the vicinity of the grain boundaries. It was also found that C was abundantly present in the V buffer layer for C added films and it was also confirmed that N was present in the vicinity of the precipitated Sm and Fe. Therefore, no grain boundary phase was formed by the addition of C and N. The detailed microstructural results will be reported in the future[13].

Since H_c was increased by the addition of B, the films were prepared by adding C and N to the B content in which H_c was improved. XRD patterns for $Sm(Fe_{0.8}Co_{0.2})_{12}$ (100 nm) thin films with B, B-C and B-N addition are shown in Fig. 9 (a). The amount of B content to $Sm(Fe_{0.8}Co_{0.2})_{12}$ thin film was fixed at 11.2 at.%, while C and N were combined added to 2.0 % and 0.2 %, respectively. The peaks from (002) and (004) of $ThMn_{12}$-type phase were clearly observed for all the films, indicating that the strongly textured structure toward (00*l*) direction was obtained. However, by the combined addition of the B-C and B-N, the intensity of the peak was significantly reduced, and the position of the peak was slightly shifted to lower angle for the film with B-C addition, while it shifted to higher angle for the film with B-N addition. The magnetization curves for $Sm(Fe_{0.8}Co_{0.2})_{12}$ (100 nm) thin films with B, B-C and B-N addition are shown in Fig. 9 (b). H_c was decreased remarkably by adding C of 2.0 % and N of 0.2 %, and the magnetic anisotropy of $Sm(Fe_{0.8}Co_{0.2})_{12}$-B thin films was changed from the out-of-plane to the in-plane anisotropy.

4. Summary

In this study, the effect of light elements such as B, C and N to the $Sm(Fe_{0.8}Co_{0.2})_{12}$ alloy was investigated. From XRD patterns, the peaks from (002) and (004) of $ThMn_{12}$-type compound were clearly observed for $Sm(Fe_{0.8}Co_{0.2})_{12}$-B thin films. High H_c of 11.1 kOe, high M_s of 1260 emu/ cm^3 and moderate high K_u of 32.2 Merg/ cm^3 were obtained for the film with B content of 11.2 at.% and t_{SFCB} of 100 nm. It was found that the B addition was very effective in improving the magnetic properties for Sm $(Fe_{0.8}Co_{0.2})_{12}$ compounds. However, no significant improvement in magnetic properties was observed with the addition of C and N to the $Sm(Fe_{0.8}Co_{0.2})_{12}$ thin film. Magnetic anisotropy was changed from the out-of-plane to the in-plane and H_c was decreased with the combined addition of C and N to the $Sm(Fe_{0.8}Co_{0.2})_{12}$-B thin films. It was confirmed that only the addition of B contributes significantly to the improvement of magnetic properties of $Sm(Fe_{0.8}Co_{0.2})_{12}$ alloy. From the results of this study, the addition of C and N is not suitable for further improving H_c in the $Sm(Fe_{0.8}Co_{0.2})_{12}$ compound. However, in order to further improve the magnetic properties of Sm $(Fe_{0.8}Co_{0.2})_{12}$ thin film, it is considered that not only the addition of B but also the grain boundary diffusion effect of the non-magnetic material plays a major role.

Acknowledgments This work was performed at the Research Institute for Engineering and Technology (High-Tech Research Center) at Tohoku Gakuin University. This work was partly supported by the Elements Strategy Initiative Center for Magnetic Materials (ESICMM) of National Institute for Materials Science (NIMS).

References

1) Y. Hirayama, Y. K. Takahashi, S. Hirosawa and K. Hono: *Scr. Mater*., **138**, 62 (2017).
2) A. M. Gabay and G. C. Hadjipanayis: *Scr. Mater*., **154**, 284 (2018).
3) B. Fuquan, J. L. Wang, O. Tegus, W. Dagula, N. Tang, F. M. Yang, G. H. Wu, E. Brück, F. R. de Boer and K. H. J. Buschow: *J. Magn. Magn. Mater*., **290-291**, 1192 (2005).
4) P. Tozman, H. Sepehri-Amin, Y. K. Takahashi, S. Hirosawa and K. Hono: *Acta Mater*., **153**, 354 (2018).
5) P. Tozman, Y. K. Takahashi, H. Sepehri-Amin, D. Ogawa, S. Hirosawa and K. Hono: *Acta Mater*., **178**, 114 (2019).
6) Y. Hirashima, K. Terakura, H. Kino, S. Ishibashi and T. Miyake: *J. Appl. Phys*., **120**, 203904 (2016).
7) I. Dirba, J. Li, H. Sepehri-Amin, T. Ohkubo, T. Schrefl and K. Hono: *J. Alloys Compd*., **804**, 155 (2019).
8) I. Dirba, H. Sepehri-Amin, T. Ohkubo and K. Hono: *Acta Mater*., **165**, 373 (2019).
9) D. Ogawa, X. D. Xu, Y. K. Takahashi, T. Ohkubo, S. Hirosawa and K. Hono: *Scr. Mater*., **164**, 140 (2019).
10) T. Fukazawa, H. Akai, Y. Harashima and T. Miyake: *J. Magn. Magn. Mater*., **469**, 296 (2019).
11) H. Sepehri-Amin, Y. Tamazawa, M. Kambayashi, G. Saito, Y. K. Takahashi, D. Ogawa, T. Ohkubo, S. Hirosawa, M. Doi, T. Shima and K. Hono: *Acta. Mater*., **194**, 337 (2020).
12) Y. Hirayama, Y. K. Takahashi, S. Hirosawa and K. Hono: *Scr. Mater*., **95**, 70 (2015).
13) H. Sepehri-Amin: *private communication* (2021).

Received Dec. 29, 2020; Accepted Feb. 22, 2021

J. Magn. Soc. Jpn., **45**, 70-74 (2021)

<Paper>

Prototype Tests of Outer-Rotor-type High-Speed PM Motor

S. Sakurai†, K. Nakamura

Tohoku University, Graduate School of Engineering, *6-6-11 Aoba Aramaki Aoba-ku, Sendai, Miyagi 980-8579, Japan*

Many kinds of servers for communication base stations are being installed to provide information technology (IT) services. Hence, the servers require not only high-performance processer but also their cooling system. Among the cooling systems, a cooling fan is the most suitable due to good balance between performance and cost. Nowadays, the cooling fans are required to be improved the cooling performance and efficiency because the heat generation in servers is increased. In a previous paper, several cooling fan motors are designed and compared each other. As a result, an interior permanent magnet (IPM) motor with the magnets equally divided in the circumference direction has the highest efficiency. This paper presents prototype test results of the proposed IPM motor, which are compared to the calculation results. Next, stray losses caused by eddy current and harmonic current are investigated by using three-dimensional finite element method (3D-FEM).

Key words: Cooling fan, interior permanent magnet (IPM) motor

1. Introduction

In communication base stations, many kinds of servers cooperatively operate to provide information technology (IT) services. According to increasing amount of information traffic, the servers and in which central processing units (CPUs) should be improved the performance, and their downsizing are also required. In order to improve the performance, increasing the clock speed of CPUs or employing the parallel processing are common ways. However, huge local heat generated in CPUs becomes serious problem along with increasing the processing performance. Therefore, cooling systems are rapidly gaining attention recently.

Among of the cooling systems, a cooling fan is widely used for removing the local heat from CPUs in the server since they have good balance between performance and cost. Recently, further improvement of the cooling performance is strongly required. To improve the performance, air flow and pressure of the cooling fan should be increased, that is, torque and rotational speed of a cooling fan motor must be increased. In addition, efficiency improvement is also important since if only the output power of the cooling fan motor is increased while the efficiency remains constant, the loss will be larger, and it causes heat generation in the fan motor itself. However, the cost has been the most important in the cooling fans so far. Thus, the efficiency of conventional cooling fan motors is low, and the reports of the efficiency improvement are very few [1]-[5].

In a previous paper, to improve the efficiency of the cooling fan motor, several kinds of rotor structures were compared each other [6]. As a result, it was clear that an interior permanent magnet (IPM) motor with the magnets equally divided in the circumference direction has the highest efficiency.

Corresponding author: S. Sakurai (e-mail: sho.sakurai.q2@dc.tohoku.ac.jp).

In this paper, prototype tests of the proposed IPM motor are demonstrated. Furthermore, stray losses caused by eddy current and harmonic current are investigated by three-dimensional finite element method (3D-FEM) using the JMAG-Designer software ver. 19.1.

2. Overview of proposed IPM motor

Table 1 shows specifications of a conventional fan motor and a target one. The rated speed of the conventional motor is 9000 rpm, the rated torque is 54 mN·m, and the efficiency at the rated point is 80%, respectively. Therefore, the total loss is 13.5 W.

Based on the conventional fan motor, to increase the air flow and pressure of the cooling fan, the target speed and torque are set to be 12600 rpm and 200 mN·m, respectively. Therefore, the output power is 256 W, which is about five times larger than the conventional one. On the other hand, the heat generation in the fan motor itself becomes problem if the loss is also five times larger. Thus, the loss target is less than 20 W, which results in the higher efficiency of 93%.

Fig. 1 shows a schematic diagram of the IPM motor proposed in the previous paper [6], and indicates the magnetization direction of the magnets. It is a three-phase, 4-pole, 6-slot machine. The stator has three-phase concentrated windings. The permanent

Table 1 Specifications of a conventional fan motor and a target one.

	Conventional fan motor	Target fan motor
Total loss (W)	13.5	20 or less
Efficiency (%)	80	93 or more
Mechanical output (W)	54	256
Rated speed (rpm)	9000	12600
Rated torque (mN·m)	57	200

magnets are divided into 5 pieces per pole and evenly arranged in the circumference direction for reduction of is sintered Nd-Fe-B. eddy current loss in the magnets. The magnet material

Here, general IPM motors have magnetic saliency to generate a reluctance torque in addition to a magnetic torque. On the other hand, as can be seen from the figure, the proposed IPM motor does not have the magnetic saliency since the magnets are uniformly embedded in the rotor core, that is, it is designed only to reduce the eddy current loss in the magnets.

Table 2 indicates specifications of the proposed IPM motor. The diameter is 54 mm. The stack lengths of the stator and the rotor are 11.9 mm and 19.5 mm, respectively.

3. Prototype test results of IPM motor

Fig. 2(a) shows the prototyped IPM motor. Since the prototype motor is an outer-rotor-type, it has an auxiliary jig so that the prototype motor can be fixed by clamping the jig between the motor mount stand as shown in Fig. 2(b).

The dc supply voltage is 48 V, which is fed to the prototype motor through a three-phase PWM converter. The motor is driven by a sensorless vector control and the current phase is controlled to be zero, namely, $i_d = 0$ control is adopted. The rotational speed is set to be 12600 rpm constant. The line voltages, the phase currents, and the input power are measured by a digital power meter. The torque and the rotational speed are measured by a torque detector. Thus, the output power can be obtained from the product of the torque and the rotational speed.

Fig. 3 shows measured and calculated speed and output power. The output power linearly increases with torque since the speed is controlled to be 12600 rpm constant.

Fig. 4 shows measured and calculated torque characteristics. The intercepts of the measured and calculated curves of the current density axis are different since the stray loss and the mechanical loss are neglected in 3D-FEM. Contrary to this, both slopes which express the torque constant of the IPM motor are almost the same.

Fig. 5 indicates measured and calculated loss characteristics. The copper loss W_c is calculated by

$$W_c = RI_{rms}^2, \quad (1)$$

where the measured winding resistance is R, whose value is also used in 3D-FEM. The root mean square value of current is I_{rms}. It is understood that the measured copper loss is larger than the calculated one because the measured current is larger than the calculated one at the same load as shown in Fig. 4. The difference of W_c at the rated torque is about 6 W.

The iron loss W_i, eddy current loss in magnets W_e, and mechanical losses W_m are difficult to be measured directly. Therefore, the sum of these losses is calculated by

$$W_i + W_e + W_m = P_{in} - P_{out} - W_c, \quad (2)$$

where the measured input power is P_{in}, the measured output power is P_{out}, respectively. On the other hand, in 3D-FEM, the iron loss W_i is calculated by using steinmetz's equation as follows:

$$W_i = A_h B_m^2 f + A_e B_m^2 f^2, \quad (3)$$

where the hysteresis loss coefficient and the eddy current loss coefficient are A_h and A_e, respectively. The maxim flux density is B_m and the frequency is f. It can be seen from Fig. 5 that the difference between measured

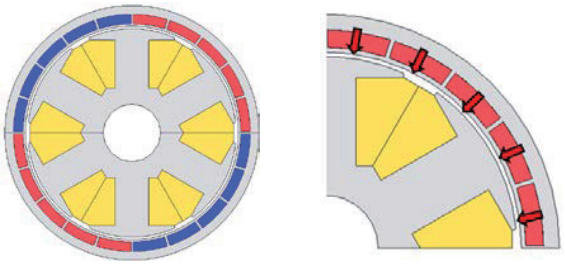

Fig. 1 Schematic diagram of a proposed IPM motor and the magnetization direction of the magnets.

Table 2 Specifications of the proposed IPM motor.

Diameter	54 mm
Stack length	Stator: 11.9 mm Rotor: 19.5 mm
Rotor speed	12600 rpm
Number of winding turns/pole	22 turns/pole
Magnet pole pairs	2
Gap length	0.5 mm
Magnet length	2.0 mm
Material of magnet	Sintered Nd-Fe-B
Material of iron	35A300

(a) Prototyped IPM motor

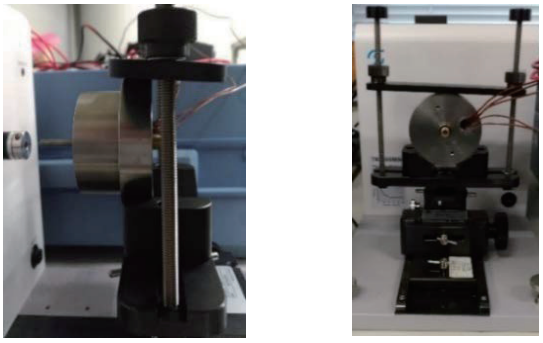

(b) Experimental setup

Fig. 2 Appearance of the prototyped IPM motor.

and calculated values is about 10W at the rated torque. The main reason is that the stray loss and the mechanical loss are neglected in 3D-FEM.

Fig. 6 denotes the measured and calculated efficiency. The calculated efficiency is given by

$$\eta = \frac{P_{out}}{P_{out}+W_c+W_i+W_e}\times 100\ (\%). \quad (4)$$

The measured efficiency at the rated torque is about 88.9%, which is higher than that of the conventional fan motor shown in Table 1. However, it is less than the calculated value of 94.1% since the stray loss and the mechanical loss are neglected in 3D-FEM.

4. Investigation of stray loss

From the above results, it was clear that the stray loss cannot be neglected. Therefore, in this chapter, the cause of the stray loss will be clarified by using 3D-FEM.

First, eddy current losses in the jig and the motor case are estimated. Fig. 7 shows the 3D-FEM model of the prototyped IPM motor including the jig and motor case. The material of these parts is stainless steel (SUS304). The stray loss is calculated using this model.

Fig. 8 shows the eddy current losses of the jig and the case. From this figure, the eddy current loss of the jig is about 2.3 W at the rated torque, while that of the case is about 0.3 W, respectively. Fig. 9 indicates the calculated efficiency considering the eddy current losses

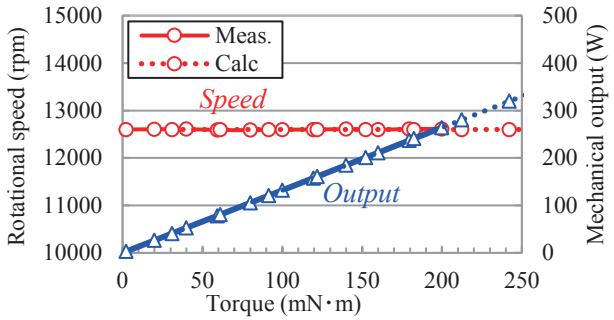

Fig. 3 Measured and calculated output characteristics.

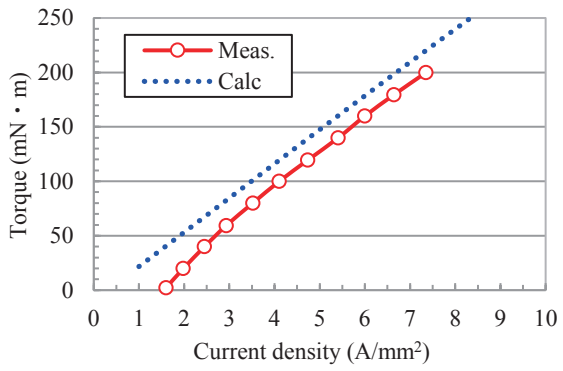

Fig. 4 Measured and calculated touque characteristics.

of the jig and the case. It is understood from the figure that the calculated values are slightly close to the measured ones, but the error is still remained.

Next, the influence of the harmonic current on the iron loss and the eddy current loss in the magnets are investigated. Fig. 10 shows the measured current waveforms at 0 mN·m and 200 mN·m, respectively. In order to consider the harmonics, the measured current waveforms are used as the input current for 3D-FEM.

Fig. 11 indicates the comparison of iron loss. It can be seen from the figure that the iron loss is increased by about 1.5 W when the harmonic current is considered.

Fig. 12 denotes the comparison of eddy current loss. It is clear that the eddy current losses of every parts are increased by the harmonic current. Especially, the magnet is affected, and its loss is increased by 0.8 W at the rated torque. The sum of eddy current losses is about 4 W at the rated torque.

As described above, since almost all the stray losses can be considered in 3D-FEM, the calculated and measured toque and efficiency are compered again.

Fig. 13 shows torque characteristics. The intercepts of the calculated and measured curves of the current density axis are almost the same since no-load loss can be estimated quantitatively.

Fig. 14 indicates loss characteristics. It is understood from the figure that the calculated copper loss is agree well with the measured ones, while the

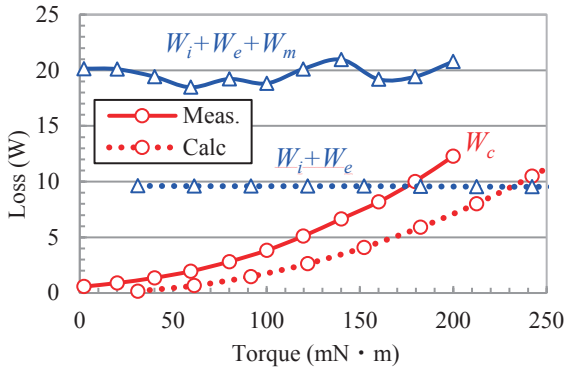

Fig. 5 Measured and calculated loss characteristics.

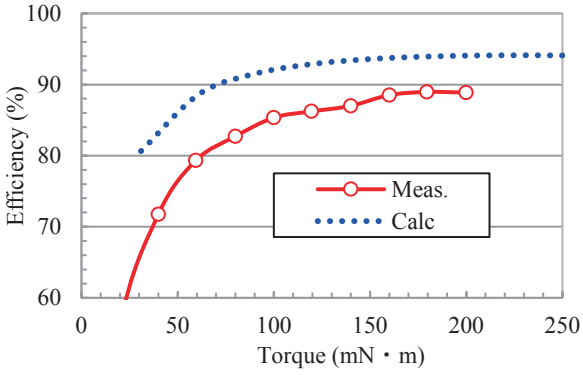

Fig. 6 Measured and calculated efficiency characteristics.

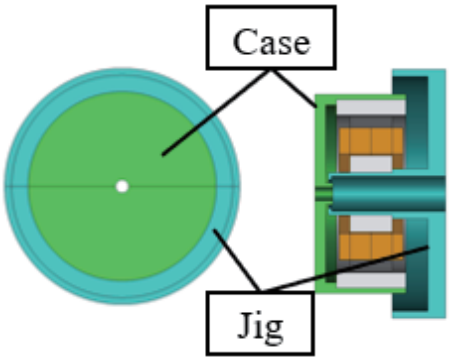

Fig. 7 Schematic diagram of the prototype motor including the jig and the motor case.

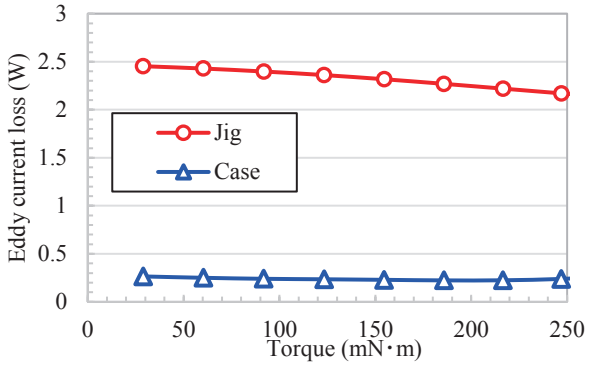

Fig. 8 Calculated eddy current losses of the jig and the motor case.

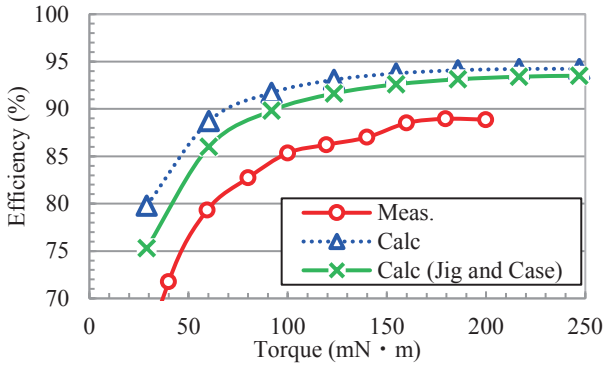

Fig. 9 Comparison of efficiency characteristics.

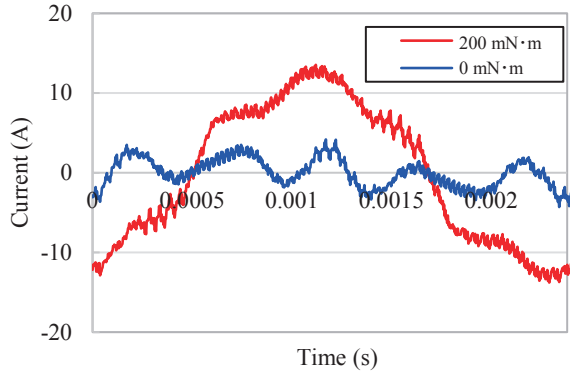

Fig. 10 Measured waveforms of the winding current.

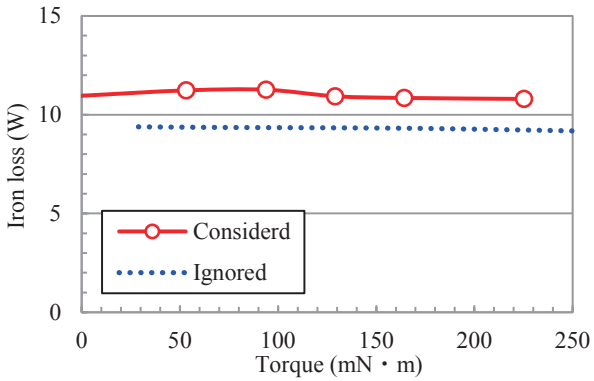

Fig. 11 Comparison of iron loss characteristics.

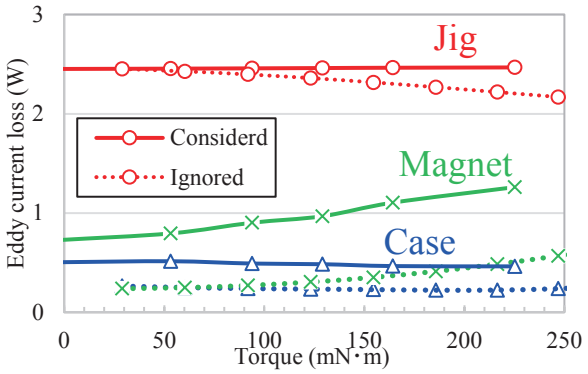

Fig. 12 Comparison of eddy current loss characteristics.

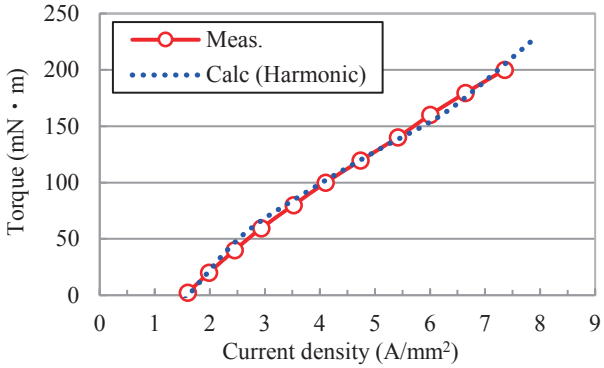

Fig. 13 Measured and calculated torque characteristics.

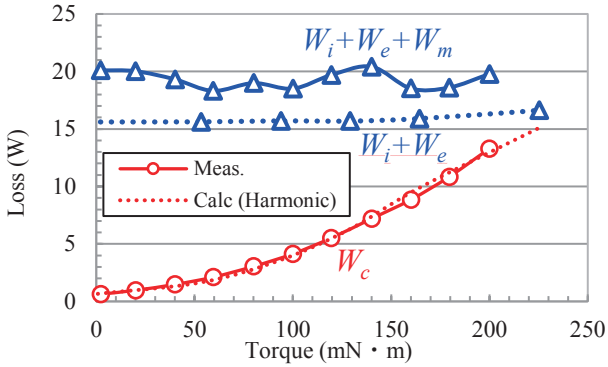

Fig. 14 Measured and calculated loss characteristics.

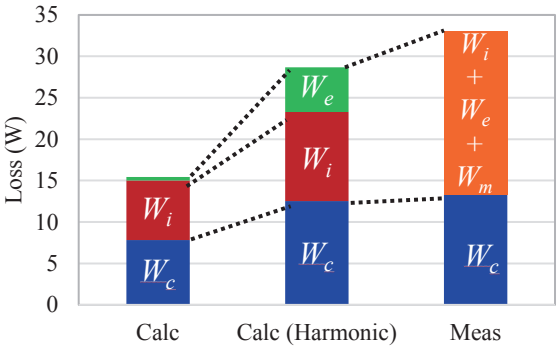

Fig. 15 Comparison of losses at the rated point.

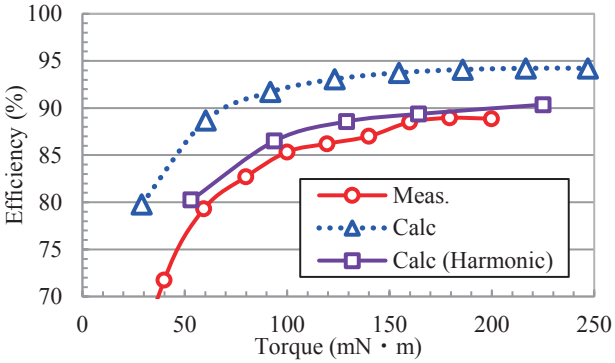

Fig. 16 Comparison of efficiency characteristics.

error is still remained in the other loss including the iron loss because the mechanical loss cannot be considered in the calculation.

Fig. 15 shows the comparison of losses at the rated point. From this figure, the calculated losses are increased by considering the harmonics. Especially, the eddy current loss in the magnets is significantly increased.

Fig. 16 denotes efficiency characteristics. It reveals that the calculated efficiency is very close to the measured ones when the stray losses are taken into consideration.

5. Conclusion

In this paper, the prototype test results of the proposed IPM motor were demonstrated and compared to the calculated ones obtained from 3D-FEM.

As a result, the measured and calculated slopes of torque curves are in good agreement, while the intercepts have an error due to the stray losses. In addition, there are relatively large difference between the measured and calculated copper and iron losses, and therefore, the calculated efficiency has an error of 5% at the rated torque.

To improve the above errors, the stray losses were investigated by using 3D-FEM. Specifically, eddy current in the jig and the motor case, and harmonic components of the winding current were considered in 3D-FEM. As a result, the calculated torque became almost the same as the measured one. Furthermore, the calculation accuracy of the copper and iron losses were also improved, and thus, the calculated efficiency was very close to the measured one.

In future works, the stray losses identified by this work will be reduced, and thereby, the efficiency will be improved to the target value of 93%.

References

1) J. F. Gieras, D. Chojnowski, and P. Mikulski, "Analysis of Steady-State and Transient Performance of Two-Phase PM Motors for Computer Fans," *IEMDC 2015*, pp. 624-629 (2015).
2) Chun-Lung Chiu, Yie-Tone Chen, You-Len Liang, and Ruey-Hsun Lian, "Optimal Driving Efficiency Design for the Single-Phase Brushless DC Fan Motor," *IEEE Transactions on Magnetics*, Vol. 46, No. 4, pp. 1123-1130 (2010).
3) A. Lelkes, J. Krotsch, R. W. De Doncker, "Low-noise external rotor BLDC motor for fan applications," *IEEE Industry Applications Society Annual Meeting*, Vol. 3, pp. 2036-2042 (2002).
4) A. Arredondo, P. Roy, and E. Wofford, "Implementing PWM fan speed control whithin a computer chassis power supply," *IEEE Applied Power Electronics Conference and Exposition*, Vol. 1, pp. 148-151 (2005).
5) Andras Lelkes, "Energy efficiency improvement in brushless fan drives," *Energy efficiency in motor driven systems*, pp. 266-275 (2006).
6) Sho Sakurai, Kenji Nakamura, "Efficiency Improvement of Outer-Rotor-type High-Speed PM Motor", Trans. Magn. Special Issues, Vol. 4, pp.72-76 (2020) (in Japanese).

Received Dec.27,2020 ; Revised Feb. 18, 2021; Accepted Mar. 10, 2021

Journal of the Magnetics Society of Japan

Vol. 45 No. 3 (通巻第315号) 2021年5月1日発行

Vol. 45 No. 3 Published May. 1, 2021
by the Magnetics Society of Japan
Tokyo YWCA building Rm207, 1–8–11 Kanda surugadai, Chiyoda-ku, Tokyo 101–0062
Tel. +81–3–5281–0106 Fax. +81–3–5281–0107

Printed by JP Corporation Co., Ltd.
Sports Plaza building 401, 2–4–3, Shinkamata Ota-ku, Tokyo 144–0054
Advertising agency: Kagaku Gijutsu-sha

発行：（公社）日本磁気学会 101–0062 東京都千代田区神田駿河台 1–8–11 東京YWCA会館 207 号室
製作：ジェイピーシー 144–0054 東京都大田区新蒲田 2–4–3 スポーツプラザビル401 Tel.（03）6715–7915
広告取扱い：科学技術社 111–0052 東京都台東区柳橋 2–10–8 武田ビル4F Tel.（03）5809–1132